Published in final edited form as:

Nature. 2020 June ; 582(7810): 124–128. doi:10.1038/s41586-020-2248-2.

Multilayered mechanisms ensure that short chromosomes recombine in meiosis

Hajime Murakami[1,*], **Isabel Lam**[1,2,†], **Pei-Ching Huang**[1,3], **Jacquelyn Song**[1], **Megan van Overbeek**[1,‡], **Scott Keeney**[1,2,3,4,*]

[1]Molecular Biology Program, Memorial Sloan Kettering Cancer Center, New York, NY 10065.

[2]Louis V. Gerstner, Jr., Graduate School of Biomedical Sciences, Memorial Sloan Kettering Cancer Center, New York, NY 10065.

[3]Weill Graduate School of Medical Sciences, Cornell University, New York, NY 10021.

[4]Howard Hughes Medical Institute, Memorial Sloan Kettering Cancer Center, New York, NY 10065.

Abstract

To segregate accurately during meiosis in most species, homologous chromosomes must recombine[1]. Small chromosomes would risk missegregation if recombination were randomly distributed, so the double-strand breaks (DSBs) initiating recombination are not haphazard[2]. How this nonrandomness is controlled is not understood, although several pathways ensuring that DSBs occur at the appropriate time, number, and place are known. Meiotic DSBs are made by Spo11 and accessory "DSB proteins," including Rec114 and Mer2, which assemble on chromosomes[3–7] and are nearly universal in eukaryotes[8–11]. Here we demonstrate how *Saccharomyces cerevisiae* integrates multiple temporally distinct pathways to regulate chromosomal binding of Rec114 and Mer2, thereby controlling the duration of a DSB-competent state. Engagement of homologous chromosomes with one another regulates the dissociation of Rec114/Mer2 later in prophase I, whereas replication timing and proximity to centromeres or telomeres influence Rec114/Mer2 accumulation early. Another early mechanism boosts Rec114/Mer2 binding specifically on the

*Correspondence to: murakamh@mskcc.org or s-keeney@ski.mskcc.org.
‡ Present address: Caribou Biosciences, Inc., Berkeley, CA 94710, USA.
† Present address: Ann Romney Center for Neurologic Disease, Department of Neurology, Brigham and Women's Hospital and Harvard Medical School, Boston, MA 02115.

Author contributions: HM performed ChIP-seq, generated translocation strains, fluorescent spore assay, and analyzed the data. PCH constructed strains for fluorescent spore assay with inducible *NDT80* and performed the assay. IL and MvO performed Spo11-oligo mapping. JS performed ChIP-seq under the supervision of HM. HM and SK conceived the project and wrote the paper. SK analyzed data, procured funding, and oversaw the research. HM, SK, and IL edited the manuscript.

Additional Information: Supplementary Information is available for this paper. Correspondence and requests for materials should be addressed to murakamh@mskcc.org or s-keeney@ski.mskcc.org.

Competing interests: Authors declare no competing interests.

Data and materials availability: All sequencing data were deposited at the Gene Expression Omnibus (GEO) with the accession numbers GSE52970 (Rec114 ChIP-seq including *tof1*), GSE84859 (Spo11 oligos in *hop1* and *red1*), GSE119786 (Mer2 ChIP-seq), GSE119787 (all Rec114 ChIP-seq generated in this study) and GSE119689 (Spo11-oligo maps in wild type at 4 and 6 h).

Code availability: All data analyses are described in Methods. Custom code for Spo11-oligo mapping is previously published and available online (references in Methods).

shortest chromosomes, subject to selection pressure to maintain hyperrecombinogenic properties of these chromosomes. Thus, an organism's karyotype and risk of meiotic missegregation influence the shape and evolution of its recombination landscape. Our results create a cohesive view of a multifaceted and evolutionarily constrained system that ensures DSB allocation to all pairs of homologous chromosomes.

Main Text:

Homologous chromosomes can only recombine if they have at least one DSB. Simulations show that the shortest chromosomes (Chr1, 3 and 6) would risk DSB failure if DSBs were random (Fig. 1a), but mechanisms attenuating this risk are apparent because chromosome size negatively correlates with crossover density[12–14], DSB density[15,16], and DSB protein binding[3,17] (Fig. 1b and Extended Data Fig. 1a). Thus, short chromosomes recruit more DSB proteins, presumably yielding higher density of DSBs and crossovers. How preferential DSB protein recruitment is achieved is unknown.

Rec114 perdures on short chromosomes

We analyzed published[18] and new meiotic timecourses of calibrated chromatin immunoprecipitation sequencing (ChIP-seq) for myc-tagged Rec114 or Mer2 (Fig. 1c, d and Extended Data Fig. 1b, c). Two key patterns emerged from relative per-chromosome abundance (Fig. 1e and Extended Data Fig. 1d, e). First, both proteins were overrepresented on short chromosomes throughout. Second, early and late ChIP densities were markedly different. Early (2–3 h), the short chromosomes had starkly higher relative ChIP densities, while the rest had low densities uncorrelated with size. Later (4–6 h), the 13 largest chromosomes showed a clear negative correlation with size and the smallest three deviated less from a linear relationship.

These patterns suggested that distinct mechanisms regulate early vs. late chromosomal binding. To test this, we measured association and dissociation times at each DSB protein peak. These times showed large early and late domains along chromosomes (Extended Data Fig. 2a). Nevertheless, Rec114 on average associated earlier and dissociated later from the shortest chromosome (chr1) than the longest (chr4) (Extended Data Fig. 2a) and this trend extended in a size-related manner across the entire complement (Fig. 1f). Importantly, per-chromosome patterns mirrored the ChIP density patterns above. The shortest chromosomes had precocious association times while the rest showed no clear size relationship, whereas dissociation times negatively correlated with size across all chromosomes, with the short trio fitting a global linear relationship (Fig. 1f).

Mean Rec114 duration correlated negatively with chromosome size, and the short trio again stood out with especially long durations (Fig. 1g and Extended Data Fig. 2b). These patterns were highly reproducible (Extended Data Fig. 2c, d) and Mer2 behaved similarly (Extended Data Fig. 2b, d).

If duration of Rec114 and other pro-DSB factors dictates how long chromosomes are DSB-competent[2,3,7,19], then Rec114 and Mer2 binding patterns should presage DSB distributions.

To test this, we measured DSBs at 4 and 6 h by sequencing Spo11 oligonucleotides (oligos), quantitative byproducts of DSBs[15]. Spo11-oligo densities correlated negatively with chromosome size, but the short trio had substantially higher density than predicted from a linear relationship (Extended Data Fig. 2e). Moreover, the 13 largest chromosomes showed a better anticorrelation at 6 h than at 4 h. Thus, DSBs mirror Rec114 and Mer2 distributions.

We infer that DSB protein association and dissociation govern size-dependent DSB control on all chromosomes and ensure overrepresentation of DSBs and crossovers on very short chromosomes. We therefore set out to elucidate this temporal regulation.

Homolog engagement dictates dissociation

DSB formation is inhibited when chromosomes engage their homologs and more effective inhibition on longer chromosomes establishes an anticorrelation between DSB density and chromosome size[2,7,16,20]. We hypothesized that: 1) distinct mechanisms control association vs. dissociation of DSB proteins; 2) shorter chromosomes take longer to engage their partners; and 3) homolog engagement displaces DSB proteins (Supplementary Discussion 1), thereby making Rec114/Mer2 duration anticorrelated with chromosome size. This hypothesis predicts that disrupting homolog engagement should not affect Rec114 binding early, but should cause inappropriate retention on larger chromosomes.

We tested this prediction in a homolog engagement-defective mutant (*zip3*)[16]. Modest differences compared to *ZIP3* in genome-wide absolute Rec114 ChIP signal at 2 and 4 h possibly reflected small differences in culture timing, but a ~;two-fold increase at 6 h was consistent with Rec114 persisting longer (Extended Data Fig. 3a–c). At 2 h and 4 h, Rec114 was overrepresented on the shortest chromosomes in *zip3*, similar to wild type (Fig. 1h and Extended Data Fig. 3b, d). At 6 h in contrast, the mutant failed to establish an anticorrelation between ChIP density and chromosome size (Fig. 1h) because of preferential Rec114 retention on larger chromosomes (Fig. 1i and Extended Data Fig. 3b, c). We conclude that feedback from homolog engagement establishes much of late-prophase DSB control by governing dissociation of Rec114 and other proteins.

Three pathways regulating association

Replication regulates Rec114 chromatin binding[18], so short chromosomes replicating early[21] might explain their early Rec114 association. We tested this by deleting origins on the left arm of chr3 (chr3L) to delay replication and using *tof1* mutation to compromise replication-DSB coordination[18]. We found that overrepresentation of Rec114/Mer2 and their early association times on short chromosomes were partially dependent on early replication (Extended Data Fig. 4a, b). Thus, replication coordination contributes but is not sufficient to explain all size differences. We inferred that additional controls exist.

To delineate these controls, we examined subchromosomal domains. Color-coded maps suggested early association and higher ChIP densities around centromeres[22] and the converse toward telomeres (Fig. 2a and Extended Data Fig. 4c, d). Fitting trend lines to all datasets and all 32 chromosome arms quantified these effects and showed how they decayed with distance (Fig. 2b, c and Extended Data Fig. 4e, f). The telomere effect may reflect a known DSB formation delay[23]. Both effects were retained in *tof1* mutants but appeared

weaker (Extended Data Fig. 4g), possibly because of constitutively early (centromeres) or late (telomeres) replication[21].

More early time points in the Mer2 data afforded a detailed look. Pericentromeric enrichment was detectable at 0.5 h, reached a maximum at 1.5 h, then diminished as Mer2 accumulation elsewhere balanced binding near centromeres (Extended Data Fig. 4h). In contrast, there was little telomere-proximal depletion of Mer2 through 1 h, then the depletion became progressively more apparent (Extended Data Fig. 4i). The centromere effect was normal in *zip3* (Extended Data Fig. 4j), consistent with homolog engagement influencing DSB protein binding late but not early.

We tested by multiple linear regression if replication timing plus centromere and telomere effects might explain DSB protein association. Regression models accounted for 37% to 51% of the variance in association timing (Fig. 2d and Extended Data Fig. 5a). Thus, a simple three-factor model gave a reasonably effective fit genome-wide (Fig. 2e). However, the model fit the shortest chromosomes poorly, with observed association earlier than predicted (Fig. 2d and Extended Data Fig. 5a, b). ChIP density at 2 h was complementary: models fit genome-wide data well but underperformed on small chromosomes by predicting less enrichment than was observed (Fig. 2f, g and Extended Data Fig. 5c, d).

Thus, for most chromosomes, DSB protein association early in meiotic prophase is shaped by replication timing and proximity to centromere or telomere. The shortest trio, however, accumulates these proteins earlier and at higher levels than these influences predict. We hypothesized that little chromosomes have an additional feature(s) boosting their ability to compete early for binding to a limited pool of DSB proteins. This idea makes two predictions if this feature is intrinsic to the DNA sequence: segments from short chromosomes should retain the boost when fused to a longer chromosome, and making an artificially small chromosome by bisecting a larger one should not be sufficient to establish a similar boost.

Boosting short chromosomes

To test if chr1 (230 kb) intrinsically boosts Rec114 binding, we artificially lengthened it by reciprocal translocation with chr4 (1.5 Mbp) (Fig. 3a and Extended Data Fig. 5e, f). We asked whether chr1 portions of derivative chromosomes (der(1) at 532 kb and der(4) at 1.2 Mb) still behaved like a short chromosome as predicted or if they now behaved like a longer chromosome as previous studies of crossing over might predict[14].

At 2 h, segments from chr1 retained Rec114 overrepresentation (Fig. 3b, left), yielding sharp ChIP transitions between chr4- and chr1-derived sequences (Fig. 3c). Moreover, a three-factor regression model again underperformed in predicting Rec114 levels on chr1-derived sequences (Extended Data Fig. 5g). These results support the hypothesis that chr1 has an intrinsic feature(s) promoting preferential early Rec114 association. This feature acts in cis and independently of chromosome size per se.

Later (4 and 6 h), translocated chr1 segments still showed Rec114 overrepresentation, but less than for native chr1 (Fig. 3b, right, and Extended Data Fig. 5h, i). Lesser Rec114

abundance matches our conclusion that feedback from homolog engagement dominates late patterns: since homolog engagement is tied to chromosome size per se, chr1-derived segments should conform to their long-chromosome context. The remaining overrepresentation relative to naturally long chromosomes may be a residuum of high early enrichment.

A converse experiment created an artificial short chromosome (177 kb) by translocation between two medium-size chromosomes. As predicted, this chromosome did not behave like a natural short chromosome in early prophase, when effects of the boost should be apparent, but did so later, when homolog engagement dominates (Extended Data Fig. 6a–f and Supplementary Discussion 2).

Selective pressure maintains the boost

Most *Saccharomyces* species have the same three short chromosomes[24]. This conservation suggests that mechanisms mitigating risk of meiotic nondisjunction are shared, implying in turn that evolutionary selection maintains hyperrecombinogenic properties of small chromosomes.

Saccharomyces mikatae provides a natural experiment for hallmarks of such selection. In other species, chr6 is the second shortest chromosome, but in *S. mikatae* the regions syntenic to ancestral chr6 (hereafter, syn6) are on longer chromosomes[24,25] (Fig. 3d). We previously showed that syn6 DSB densities match the chromosomal context, but inferred that density is tied to chromosome size and not DNA sequence[26]. To revisit this conclusion, we reasoned that lack of selective pressure to maintain a DSB protein-binding boost on syn6 during post-translocation generations would lead to absence of the boost in extant *S. mikatae* strains. Chr1 should preserve the boost because it is still small.

As predicted, chr1 in *S. mikatae* showed strong overrepresentation of Rec114 at 2 h, but Rec114 binding was lower on syn6 in *S. mikatae* than for chr6 in *S. cerevisiae*. Indeed, syn6 segments were indistinguishable from larger chromosomes (Fig. 3e, left, and Extended Data Fig. 6g). A three-factor regression model fit syn6 data well but still underperformed for chr1 (Extended Data Fig. 6h). Later (4 and 6 h), syn6 segments had relative Rec114 densities in line with their chromosome sizes (Fig. 3e, right, and Extended Data Fig. 6i, j).

The boost requires axis proteins

Meiotic chromosomes form axial structures anchoring chromatin loops[27]. Because DSB proteins assemble on axes, arranging a DNA segment as short loops on a long axis is proposed to yield higher DSB density than if arrayed as long loops on a short axis[28–30]. Analysis of published data[31] showed that chr3 has a ~;1.2 fold larger axis:DNA ratio (3.89 μm/Mbp on average) than chr4 or chr15 (3.22 μm/Mbp; Extended Data Fig. 7a), although densities of preferred DSB protein binding sites were not different between small and large chromosomes (Extended Data Fig. 7b). These findings are consistent with loop-axis structure contributing to intrinsic DSB potential.

Axis proteins Hop1, Red1, and Rec8 promote normal chromatin association of Rec114 and Mer2, and Hop1 and Red1 are overrepresented on short chromosomes, suggesting that axis

protein enrichment contributes to high DSB density[3,17]. To test this hypothesis, we assessed Rec114 ChIP density and DSB formation in axis mutants.

Both *hop1* and *red1* single mutants eliminated Rec114 overrepresentation on small chromosomes early (2 h) and ablated the anticorrelation of Rec114 binding with chromosome size at all times (Extended Data Fig. 7c). Both mutations greatly decreased Rec114 ChIP levels genome-wide[3], but, unexpectedly, Rec114 binding was substantially higher in a *hop1 red1* double mutant without rescue of either the DSB defects or Rec114 spatial patterns (Fig. 4a, Extended Data Fig. 7d–g, and Supplementary Discussion 3). Even with this more robust ChIP signal, short chromosomes still lacked Rec114 overrepresentation at 2 h, and only a weak size dependence emerged later (Fig. 4b and Extended Data Fig. 7c).

Absence of Rec8 did not eliminate relative enrichment of Rec114 on short chromosomes (Extended Data Fig. 7c)[17], although total Rec114 binding was greatly reduced (Fig. 4a). A *hop1 red1 rec8* triple mutant behaved like *hop1 red1*: improved Rec114 recruitment but no short-chromosome boost (Fig. 4a, b). Rec8, which is enriched at centromeres[22,32], was required for preferential Rec114 binding near centromeres but Hop1 and Red1 were not (Extended Data Fig. 7h).

Spo11-oligo maps demonstrated functional significance of loss of Hop1 and Red1: mutants lacked any higher density of DSBs on short chromosomes (Fig. 4c). Instead, an inverted relationship of DSBs with chromosome size suggested complete loss of size-dependent control. These findings implicate the chromosome axis as a platform supporting DSB regulation.

Safeguarding chromosome segregation

Early in prophase, three mechanisms (replication timing and distances to centromere and telomere) govern spatial and temporal patterns of Rec114 and Mer2 binding to all chromosomes and a fourth mechanism(s) boosts binding on the smallest chromosomes (Fig. 4d). Each mechanism differs in magnitude and contributes differently to chromosome size dependence (Fig. 4e and Supplementary Discussion 4). Another pathway (homolog engagement) primarily regulates DSB protein dissociation (Fig. 4d, Extended Data Fig. 7i and Supplementary Discussion 4). Within the context of homolog engagement, a tendency for chromosome end-adjacent regions to prolong DSB formation[33] contributes modestly compared to other feature(s) such as size-dependent pairing kinetics (Extended Data Fig. 8, 9 and Supplementary Discussion 5, 6).

We propose that these pathways collaborate to govern the amount of DSB protein binding and the duration of a DSB-permissive state, thus shaping per-chromosome and within-chromosome “DSB potential” (Supplementary Discussion 7). The early pathways proactively establish when chromosomal segments become competent to make DSBs, so they modulate the population-average DSB probability. In contrast, feedback from homolog engagement reacts to a favorable outcome, so it not only affects the population-average DSB probability, it also ensures a low failure rate by allowing DSB formation to continue until

success is achieved. Regulatory circuits involving Tel1^{ATM} and Mec1^{ATR} further ensure success[2,7,34–37].

The purpose of this pathway integration is presumably to assure every chromosome the opportunity to pair and recombine. To test this idea, we disrupted reactive pathways by inducing premature prophase I exit with an exogenously controlled Ndt80 transcription factor (Supplementary Discussion 8). As predicted, early Ndt80 induction increased the frequency of meioses in which the artificial short chromosome (der(9)) was non-exchanged and suffered meiosis I nondisjunction (Extended Data Fig. 10a–c). Accurate segregation of a naturally short chromosome (chr6) was more sensitive to premature prophase exit than a mid-sized chromosome (chr5), and der(9)—which lacks the boost—was more sensitive still (Fig. 4f and Extended Data Fig. 10d, e).

Targeted boosting of DSB protein binding, perhaps by organizing short loops on long axes, may be a versatile strategy to mitigate meiotic missegregation risk caused by karyotypic constraints, for example restriction of sex chromosome recombination to the pseudoautosomal region in mammalian males[28] (Supplementary Discussion 9 and Extended Data Fig. 10f). Budding yeast's multilayered control provides a paradigm for how cells solve the challenge of ensuring recombination on every chromosome, no matter how small.

Methods

Yeast strain and plasmid construction

Myc-epitope tagging of Rec114 and Mer2 in S. cerevisiae and S. mikatae—To perform ChIP-seq experiments in *S. cerevisiae*, Rec114 or Mer2 were C-terminally tagged with 8 and 5 copies of the Myc-epitope marked with the *hphMX4* cassette and the *URA3* gene, respectively (*REC114-Myc* and *MER2-Myc*), described in refs[18,40]. Rec114 in *S. mikatae* was C-terminally tagged with the Myc-epitope with the same construct used to tag Rec114 in *S. cerevisiae*. Epitope tagged Rec114 in *S. mikatae* was checked by western blotting and was functional as the *REC114-Myc* strain showed good spore viability (98%, 16 tetrads).

Targeting reciprocal translocation between chr1 and chr4—Reciprocal translocation between chr1 and chr4 was targeted as described in Extended Data Fig. 5e. The *TRP1* gene with a 3′ portion of the *K. lactis URA3* gene (*Kl.URA3*) was amplified from plasmid pWJ716[48] using primers TL#1AF and TL#1AR (Supplementary Table 1), which each contain 50 nt from the terminator region of *SWC3* in the left arm of chr1. The *HIS3* gene with a 5′ portion of *Kl.URA3* was amplified from pWJ1077[48] using primers TL#1BF and TL#1BR (Supplementary Table 1), which each contain 50 nt from the terminator region of *SLX5* in the left arm of chr4. Each amplified DNA fragment was transformed into *MAT***a** and *MATα* haploid yeast (*ura3, trp1, his3*), respectively. After verifying transformants by PCR and sequencing, *MAT***a** and *MATα* transformants were mated. Since the two *Kl.URA3* segments share identical sequence (448 bp), homologous recombination between these regions would produce uracil prototrophy along with reciprocal translocation between chr1 and chr4. We sporulated the diploid and screened for Ura+ haploids by spreading spores on SC-ura plates. A Ura+ haploid was verified by pulsed-field gel electrophoresis (PFGE)

followed by Southern blotting using probes hybridizing to both ends of chr1 and chr4 generated by primers listed in Supplementary Table 1 (see Extended Data Fig. 5f for an example). We confirmed that native chr1 and chr4 had disappeared and derivative chromosomes der(1) and der(4) of the expected size had appeared. The verified haploid was crossed with a *REC114-myc* haploid which retains native chr1 and chr4 to isolate both mating types with der(1), der(4) and *REC114-myc.* These haploids were verified by Southern blotting again and mated to obtain a diploid with the homozygous translocation in the *REC114-myc* background.

Targeting reciprocal translocation between chr8 and chr9—Reciprocal translocation between chr8 and chr9 was targeted by CRISPR/Cas9 as described in Extended Data Fig. 6a. Two guide RNA sequences were cloned into pCRCT (*URA3*, iCas9, 2 micron ori)[49] to target cleavages in the downstream regions of *YHL012w* (80468: chr8, left arm) and *URM1* (342918, chr9, left arm). The plasmid was cotransformed with 100-bp recombination donor fragments that have translocated sequences into a *MATα REC114-myc* haploid. Ura+ transformants were first screened on SC-ura plates and then checked for translocation by PCR with primer pairs flanking the two junctions. Positive transformants were mated with a wild type *MATa* haploid. The resulting diploid turned out to be homozygous for the translocated chromosomes probably because of recombination induced by Cas9 cleavages using der(8) and der(9) as template. The sizes of the translocated chromosomes in the above haploids and diploids were confirmed by PFGE followed by Southern blotting using probes hybridizing to both ends of chr8 and chr9 generated by primers listed in Supplementary Table 1 (Extended Data Fig. 6b). Diploids that had lost the plasmid were selected on 5-FOA plates and subjected to sporulation followed by tetrad dissection to isolate *MATa* and *MATα* haploids with der(8), der(9), and *REC114-myc*. These haploids were mated and the resulting diploid was used for further experiments.

Axis mutants—The *red1*, *hop1*, and *mek1* deletions were made by replacing the respective coding sequences with the hygromycin B drug resistance cassette (*hphMX4*) amplified from plasmid pMJ696 (identical to pAG32[50]). Yeasts were transformed using standard lithium acetate methods. Gene disruption was verified by PCR and Southern blotting. The *SPO11-Flag* construct (*SPO11-6His-3FLAG-loxP-kanMX-loxP*) was provided by Kunihiro Ohta, Univ. Tokyo[22]. All axis (*hop1, red1, rec8, hop1 red1*, and *hop1 red1 rec8*) and *zip3* mutants in the *REC114-Myc* background were created by multiple crossing followed by tetrad dissection.

Plasmids for spore-autonomous fluorescent markers—Plasmids pSK1269 ($P_{YKL050c}$*-GFP*-KanMX*) and pSK1271 ($P_{YKL050c}$*-CFP-natMX*) were constructed by subcloning EcoRI fragments from pSK726 and pSK692[39] into EcoRI sites on pFA6a-KanMX[51] and pMJ695 (identical to pAG25[50]), respectively. Fluorescent markers and drug resistant cassettes are tandem orientation. For the RFP integration into the right arm of chr9, a 247 bp sequence within the downstream of YPS6 ORF was amplified using primers (inf9RightRFPF and inf9RightRFPR) listed in Supplementary Table 1 and cloned at the Tth111I site in pSK691 ($P_{YKL050c}$*-RFP-LEU2*) using In-Fusion HD (TaKaRa), yielding an integrative plasmid (pSK1320).

Construction of strains with inducible NDT80 and spore-autonomous fluorescent markers—To introduce the inducible *NDT80* system, a *GAL4-ER* P_{GAL}-*NDT80* strain (from Angelika Amon, MIT)[52] was crossed with our strain with der(9). Resulting haploids from tetrad dissection were transformed with spore-autonomous fluorescent markers with 50 bp homology sequence amplified from pSK1269, pSK1271 or pSK691[39]. Transformants were checked by PCR designed at two junctions as following combination (integration marker and locus: primers to amplify marker; plasmid; primers to check integration). RFP at *MSH4* downstream (cen6): TF_RFP_cen6F/R; pSK691; cen6_RFP_check1F/cen1_RFP_check1R and cen1_RFP_check2F/cen6_RFP_check2R. GFP at *NAS2* downstream (translocation junction, cen9): TF_GFP_cen9v3F/R; pSK1269; cen9_GFP_check3F/ cen9_GFP_check1v2R and cen9_GFP_check2F/cen9_GFP_check3R. CFP at *GIM4* downstream (cen5): TF_CFP_cen5F/R; pSK1271; cen5_CFP_check1F/R and cen5_CFP_check2F/R. CFP at *YHL048w* downstream (chr8L): TF_CFP_chr8LF/R; pSK1271; chr8L_CFP_check1F/R and chr8L_CFP_check2F/R. RFP integration at *YPS6* (chr9R) was done by integrating pSK1320 linearized with NdeI and transformants were checked by PCR using chr9R_RFP_check1F/R and chr9R_RFP_check2F/R. Strains with appropriate marker configuration (Extended Data Fig. 10 and Supplementary Table 2) were created by crossing the above transformants followed by tetrad dissection.

Yeast growth conditions

Studies were performed using *S. cerevisiae* SK1 and *S. mikatae* IFO1815 strain backgrounds; strains are listed in in Supplementary Table 2. Synchronous meiotic cultures were with the SPS pre-growth method[47]. Briefly, saturated overnight cultures in 4 ml YPD (1% yeast extract, 2% peptone, 2% glucose) were used to inoculate 25 ml of SPS (0.5% yeast extract, 1% peptone, 0.67% yeast nitrogen base without amino acids, 1% potassium acetate, 0.05 M potassium biphthalate, pH 5.5, 0.002% antifoam 204 (Sigma)) to a density of 5×10^6 cells/ml and cultured at 30°C at 250 rpm for 7 h. Cells were then inoculated into an appropriate volume (900 ml for ChIP-seq experiments with 12 time points or 300 ml for experiments with 3 time points) of fresh SPS at a density of 3×10^5 cells/ml and cultured at 30°C at 250 rpm for 12–16 h until the density reached 3–4 × 10^7 cells/ml. Cells were collected by filtration, washed with water, then resuspended at 4×10^7 cells/ml in appropriate volume (610 ml for 12 time points or 200 ml for 3 time points) of SPM (2% potassium acetate, 0.001% polypropylene glycol) supplemented with 0.32% amino acid complementation medium (1.5% lysine, 2% histidine, 2% arginine, 1% leucine, 0.2% uracyl, 1% tryptophan). Cultures were shaken at 250 rpm at 30°C and 50 ml samples for ChIP-seq were collected at desired times after transfer to SPM. For 12-time-point cultures, we collected samples as follows: 0, 2, 2.5, 3, 3.5, 4, 4.5, 5, 5.5, 6, 7, 8 h for Rec114 ChIP in *TOF1* background; 0, 1, 1.5, 2, 2.5, 3, 3.5, 4, 4.5, 5, 6, 7 h for Rec114 ChIP in *tof1* background; 0, 0.5, 1, 1.5, 2, 2.5, 3, 3.5, 4, 4.5, 5, 6 h for Mer2 ChIP. For all 3-time-point cultures, cells were collected at 2, 4 and 6 h.

For the Spo11-oligo mapping experiments, synchronous meiotic cultures of *S. cerevisiae* SK1 were prepared as described in ref.[53]. Briefly, cells from a saturated overnight YPD culture were used to inoculate a 14-h pre-sporulation culture in YPA (1% yeast extract, 2% peptone, 1% potassium acetate) supplemented with 0.001% antifoam 204 and grown at 30°C

(starting cell density (OD_{600}) of 0.2). Cells were harvested, resuspended in 2% potassium acetate, 0.2 × supplements (2 μg/ml adenine, 2 μg/ml histidine, 6 μg/ml leucine, 2 μg/ml tryptophan, 2 μg/ml uracil), 0.001% antifoam 204 at OD_{600} = 6.0, and incubated in a 30°C shaker to induce sporulation.

To assess culture synchrony, meiotic division profiles were obtained by collecting aliquots at various times from synchronous meiotic cultures, fixing in 50% (v/v) ethanol, and staining with 0.05 μg/ml 4′, 6-diamidino-2-phenylindole (DAPI). Mono-, bi- and tetranucleate cells were scored by fluorescence microscopy.

Chromatin immunoprecipitation for Mer2-Myc and Rec114-Myc

We performed ChIP experiments as described previously[18], with modifications in cell disruption and chromatin fragmentation. Cells were disrupted by vigorous shaking at 6.5 m/s for 1 min × 10 times in a FastPrep24 (MP Biomedicals). Chromatin in the whole cell extracts (WCE) was sheared by sonication with “M” intensity, 30 sec ON/ 30 sec OFF for 15 min × 3 times in a Bioruptor Sonication System UCD200 (Diagenode) in 15 ml polystyrene conical tubes. Insoluble fraction (cell debris) was removed by centrifugation at 21,130 *g*, 5 min, 4°C. WCE was further sonicated with the same conditions 3–5 times to yield average DNA size less than 500 bp.

For qPCR, we used eight and ten primer pairs for *S. cerevisiae* 12-time-point and 3-time-points datasets, respectively. For *S. mikatae* we used ten primer sets. All primer sets are listed in Supplementary Table 1. qPCR was performed using the LightCycler® 480 SYBR Green I Master (Roche) according to manufacturer recommendations. All measurements of ChIP samples were expressed relative to the standard (dilution series of corresponding input samples).

Spo11-oligo mapping

For Spo11-oligo mapping, ≥ 600 ml sporulation culture volume was harvested 4 h after transfer to sporulation media. Because of the severe DSB defect in *red1* and *hop1*, Spo11 oligos from multiple (4–5) cultures of independent colonies were pooled to generate each Spo11-oligo map. The wild-type Spo11-oligo map in Fig. 4c was from a previous study[38].

Spo11-oligo mapping in *red1* and *hop1* mutants was performed essentially as described previously[26], with modifications to purify enough Spo11 oligos from *red1* and *hop1* strains. For example, Spo11 oligos from independent cultures were pooled after eluting from the first immunoprecipitation and at the last step of oligo purification (after proteinase K treatment and ethanol precipitation of the oligos). When pooling Spo11-oligo complexes from five cultures after the first immunoprecipitation step, the total volume of the second immunoprecipitation was increased to 4 ml, and 500 μl of Dynabeads Protein G slurry were pre-bound to 100 μl of 1 mg/ml anti-Flag antibody (as opposed to 125 μl of Dynabeads Protein G slurry pre-bound to 25 μl 1 mg/ml anti-Flag antibody, and a 2nd IP volume of 800 μl). Purified Spo11 oligos were quantified and used for library preparation as described previously[16].

Sequencing (Illumina HiSeq 2500, 2 × 75 bp paired-end reads) was performed in the MSKCC Integrated Genomics Operation. Clipping of library adapters and mapping of reads was performed by the Bioinformatics Core Facility (MSKCC) using a custom pipeline as described[15,16,26,38,54]. Reads were mapped to the sacCer2 genome assembly of type strain S288C from SGD (*Saccharomyces* Genome Database).

ChIP-seq data processing: scaling and masking

ChIP-seq experiments were performed as described[18]. DNA from ChIP and input samples (same samples as used for ChIP-qPCR) were further sheared by sonication to an average fragment size of ~;300 bp. These were sequenced (50 bp paired-end) on the HiSeq platform (Illumina). Reads were mapped to the SacCer2 genome assembly and *S. mikatae* genome assembly[55] using BWA (0.7) MEM to generate coverage maps for each time point from each strain. Each ChIP coverage map was divided by the corresponding input map for normalization. Then, to scale the ChIP-seq coverage relative to absolute ChIP efficiency, we calculated the total coverage within ± 1 kb of the center of each qPCR amplicon, plotted these as a function of the corresponding qPCR ChIP efficiency, and calculated regression lines by least squares. The resulting regression line for each time point was then used to scale the ChIP-seq coverage maps.

To remove regions with spurious mapping, we previously defined “mask regions” where the coverage from the 0 h sample of the wild-type *ARS*+ strain was out of a fixed range (>1.5 SD from mean coverage) with further extension by 1 kb on either side[18]. These regions were censored in all input and ChIP coverage maps from *S. cerevisiae*. Mask regions for *S. mikatae* were defined similarly where the coverage from the 2 h input sample exceeded a fixed range (mean coverage ± 4 SD, calculated between 50–150 kb region of chr1). After the same extension, these regions were censored from *S. mikatae* coverage maps.

Replication index generated by ChIP input coverage maps

All masked coverage maps from input samples were binned using 5 kb windows and normalized to genomic mean coverage. For 12-time-point datasets, coverage from an “S-phase time point” (1.5 h and 2.5 h for Rec114 ChIP *ARS+ tof1*Δ and Rec114 ChIP *arsΔ tof1*Δ, respectively; 2 h for the rest) was divided by the corresponding “G1-phase time point” (0-h sample) to generate a “relative coverage” map. For 3-time-point datasets, the 2-h time point map was divided by the 0 h map from the Rec114 ChIP *ARS*+ dataset to generate relative coverage. For the *S. mikatae* dataset, the mean normalized 2 h map was used as relative coverage. We defined the “replication index” as $-\log_2$(relative coverage). Outliers were removed from each dataset, defined as the replication index value exceeding a fixed range (mean ± 4 SD).

Estimating association and dissociation times by sequential curve fitting

The method to measure association time is described in ref.[18]. The scaled and masked ChIP-seq coverage maps from two Rec114 ChIP-seq and Mer2 ChIP-seq data sets were smoothed using a 2010-bp Parzen (triangular) sliding window. Using the smoothed, scaled coverage map at 3.5 h time points, a total of 1477 (Rec114 ChIP *ARS*+), 1545 (Rec114 ChIP *ars*Δ) and 1550 (Mer2 ChIP) peaks were called using as a threshold of 0.5× each chromosome’s

mean coverage. A ChIP temporal profile at each peak position was assembled by collecting the ChIP signals from the smoothed, scaled coverage map for each time point.

To define the empirical maximum time in the ChIP profile (t_{max}), Gaussian curves were fitted to ChIP signals plotted as a function of time. To create positive skew in the regression curves, times (t, in hours) were log-transformed [$t' = \ln(t+1)$]. We employed an equation that is a modification of the Gaussian probability density function:

$$y = a + b \times e^{-\frac{(t' - c)^2}{d^2}}$$

where y is ChIP signal, a is the background, b is the peak height, c is the peak position, and d is the equivalent of standard deviation. We set the background parameter (a) to the ChIP signal at 0 h, then fitted the equation to the data points by least squares to estimate the other parameters (b, c and d) using the "nls" function in R. The estimated parameter (c) was transformed back to hours in meiosis ($t_{max} = e^c - 1$).

Next, to estimate the association time of DSB protein, we used this peak to fit a saturating exponential growth (logistic) curve to just the upward slope of the ChIP temporal profile (data points before t_{max}):

$$y = a + \frac{b}{1 + e^{c(d - t)}}$$

where y is ChIP signal, a is the background, b is the maximum value, c is a shaping factor and d is the inflection point of the logistic function, respectively. We set the background and the maximum value parameters (a and b) to the ChIP signal at 0 h and the previously estimated peak height value (parameter (b) from skewed Gaussian fitting, b_{Gauss}), respectively, and then fitted the equation to the data points to estimate the other parameters (c and d) using the "nls" function in R. We used d as $t_{association}$ where the logistic curve reaches 50% of maximum.

We also estimated the dissociation time of DSB protein by fitting a logistic curve to the downward slope of the ChIP temporal profile (data points after t_{max}):

$$y = a + \frac{b}{1 + e^{c(t - d)}}$$

where y is ChIP signal, a is the background, b is the maximum value, c is a shaping factor and d is the inflection point of the logistic function, respectively. We used the "nls" function to estimate parameters (c and d) and used d as $t_{dissociation}$ where the logistic curve reaches 50% of maximum.

To evaluate the fitting quality for the kinetic profile at each peak, absolute distances between the data points and the fitted Gaussian curve (residuals) were summed and divided by the peak height (parameter b_{Gauss}) from the fitted curve (normalized-total residuals, r_{Gauss}).

Total residuals from two logistic fittings were divided by b_{Gauss}, and the sum of these was defined as r_{logistic}. We excluded poorly fitted peaks with normalized residuals exceeding 1.2 for Rec114 ChIP *ars*Δ and Mer2 ChIP datasets. We used less stringent criteria (filtering out peaks with $r_{\text{Gauss}} > 1.6$ or $r_{\text{logistic}} > 1.5$) for Rec114 ChIP *ARS*+ dataset because overall quality of fittings was less good compared to the other two datasets. After these filtering steps, totals of 998 (Rec114 ChIP *ARS*+), 1081 (Rec114 ChIP *ars*Δ), and 1490 (Mer2 ChIP) peaks were processed for further analyses.

For the Rec114 association time in the two *tof1* datasets, we used previously estimated values for 957 (*tof1 ARS*+) and 2020 (*tof1 ars*Δ) peaks that passed filtering[18].

Estimating centromere and telomere effects on DSB protein association and dissociation time, and ChIP density at 2 and 6 h

Association and dissociation timing, and ChIP density (2 and 6 h) data from the two Rec114 and one Mer2 ChIP time courses were combined as follows. To capture the intra-chromosomal features separate from inter-chromosomal differences, we averaged each dataset in 20-kb bins, standardized the values for each chromosome to a mean of 0 and variance of 1, and standardized again within a dataset before pooling all datasets together. The first standardization minimizes differences between chromosomes and the second standardization minimizes differences between datasets. The pooled association, dissociation time or ChIP density (2 or 6 h) data were plotted as a function of distance from centromere or telomere. We fitted an exponential decay model to these data points:

$$y = \frac{a}{e^{x/b}} + c$$

where y is association time, dissociation time, or ChIP density at 2 or 6 h, x is distance from centromere or telomere, a is the initial value of the centromere or telomere effect, b is a shaping factor and c is the intercept, respectively. We used the “nls” function in R to estimate parameters (a, b and c) and used the parameter (b) to present the half distance where the initial value decays to half as the following:

$$Half\ distance = b \times \ln(2)$$

For the telomere effect modeling of ChIP density at 6 h, to represent DSB protein repression within 20 kb from telomere and enrichment in the adjacent regions (~;100 kb), we fitted a composite model consisting of two exponential decay models:

$$y = \frac{a}{e^{(x/b)}} + \frac{a'}{e^{(x/b)'}} + c$$

where y is ChIP density at 6 h, x is distance from telomere, a and a' are the initial values of the repression and enrichment effects, b and b' are shaping factors and c is the intercept.

Multiple linear regression analysis

To perform multiple regression analyses, replication index, association time, dissociation time, and ChIP density at 2 or 6 h were averaged in 20-kb bins. Distances from centromere and telomere at the midpoints of the 20-kb bins were plugged into the centromere and telomere exponential models whose parameters were estimated as described in the preceding section. The same centromere and telomere models were used for multiple regression in strains with translocation and in *S. mikatae*. Regression coefficients and the standardized regression coefficients (beta) are shown along with *t* and *P* values based on the standardized coefficients in Supplementary Tables 3–5.

Fluorescent spore assay to measure crossing over and MI nondisjunction

Diploids with der(9), spore-autonomous fluorescent markers and inducible *NDT80* (SKY7023 and 7034) were sporulated using the SPS presporulation method described above. One ml SPM culture was removed at the indicated times in Fig. 4f and Extended Data Fig. 10c and returned to the shaker after adding β-estradiol (SIGMA, 1 μM final). Cells were harvested 54 h after transfer to SPM and 200 (SKY7023) and more than 500 (SKY7034) tetrads per time point were scored as previously described[39]. We used 40× objective lens and analyzed the captured tetrad images using Fiji[56]. We scored only tetrads with four obvious spores. For tetrads where fluorescent signals in spores was difficult to call positive or negative from visual inspection, we quantified signal strength of spores within a tetrad and called a given spore positive if its signal exceeded two (RFP and CFP) or four (GFP) fold higher than a sister spore with lower signal. Tetrads with aberrant numbers of "positive" spores other than two positive (SKY7023) and two or four positive (SKY7034) were excluded for further analysis.

For the strain designed to detect crossovers, nonexchange chromosomes (E0), and MI nondisjunction (MINDJ) on der(9) (SKY7023, Extended Data Fig. 10a, b), 200 tetrads per time point were scored. Tetrads with an aberrant number of positive spores other than two positive were excluded (marker gain or loss in Supplementary Table 6). The rest of tetrads were categorized as listed. The number of crossovers was estimated for each interval using the equation, TT + 6NPD, where TT is tetratypes and NPD is nonparental ditypes. Since MI nondisjunction and double NPD events would produce tetrads with identical fluorescent signal pattern (Extended Data Fig. 10b), the number of MINDJ was corrected as observed MINDJ – fraction($NPD^{CFP\text{-}GFP}$)*fraction($NPD^{GFP\text{-}RFP}$)*(total number of tetrads). Similarly, the number of E0 was corrected as observed E0 + fraction($NPD^{CFP\text{-}GFP}$)*fraction($NPD^{GFP\text{-}RFP}$)*(total number of tetrad). Based on the assumption that most MINDJ events are also E0, the total E0 was estimated as the sum of corrected E0 and corrected MINDJ. We also independently estimated E0 assuming a Poisson distribution of crossovers in the population of cells with the measured average crossover number (dashed line in Extended Data Fig. 10c). Because the two ways of estimating E0 values agreed well, we conclude that these measurements are robust.

For the strain designed to detect MINDJ on der(9), chr6, and chr5 (SKY7034, Extended Data Fig. 10d, e), more than 500 tetrads per time point were scored. Tetrads with two

positive and two negative fluorescent spores were counted as MINDJ (Supplementary Table 7). We did not score tetrad showing other than four or two positive spores.

Extended Data

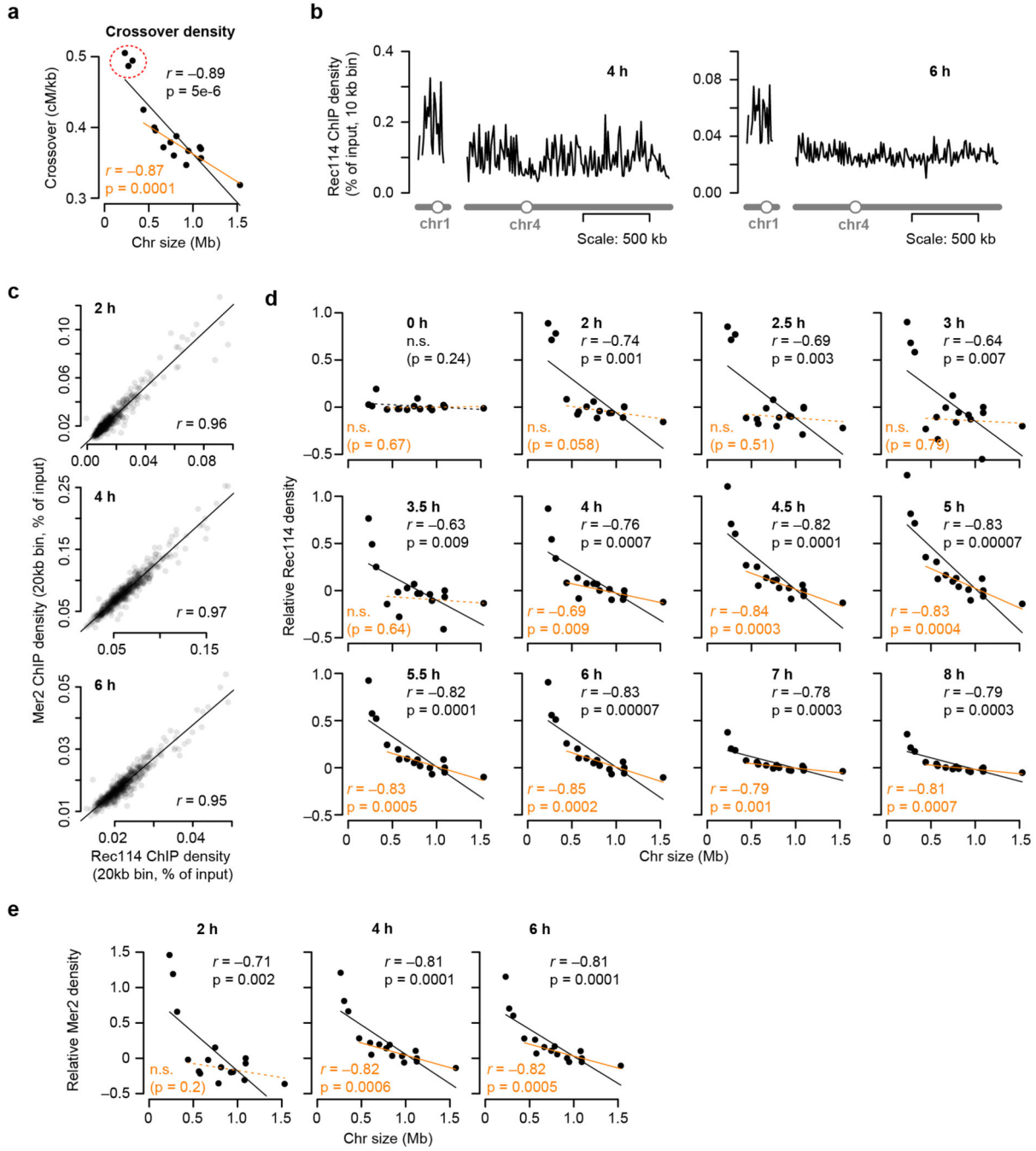

Extended Data Figure 1. Chromosome size dependence of DSB protein binding

a, Chromosome size dependence of crossovers (centiMorgans (cM) per kb). Data are from ref [12]. n = 51 tetrads.

b, Example Rec114 ChIP-seq profiles for chr1 and chr4 at 4 h and 6 h.

c, Similarity of Rec114 and Mer2 ChIP-seq patterns. Both strains are *ars*Δ background, where all active replication origins on the left arm of chr3 are deleted. Similar profiles of both proteins suggest similar regulation. n = 1 time course for each strain.

d, Full time course of average per-chromosome Rec114 ChIP densities (*ARS*+ strain). n = 1 time course.

e, The size dependence of average per-chromosome Mer2 ChIP density changes over time similar to Rec114 (compare to Fig. 1e). n = 1 time course.

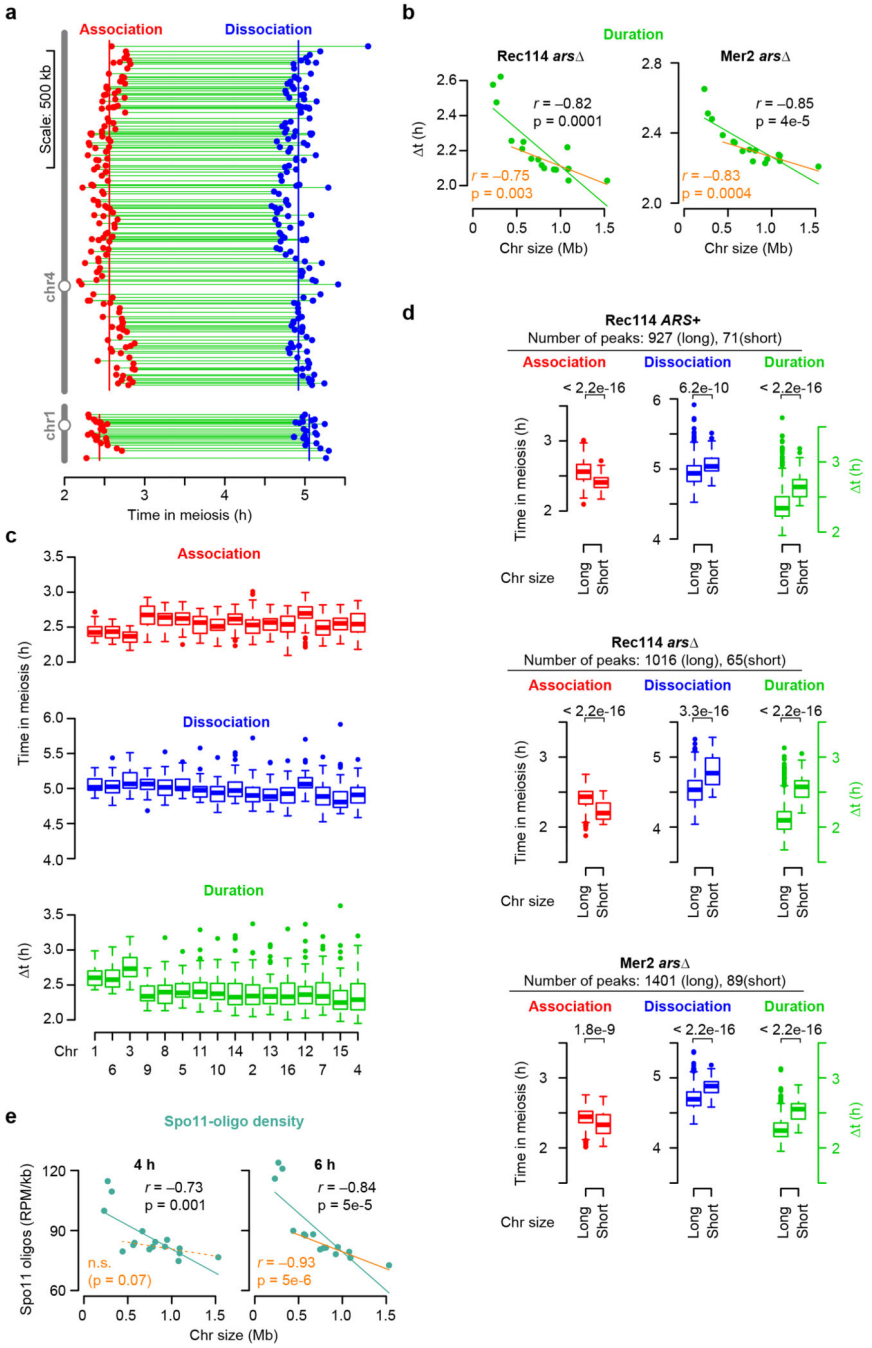

Extended Data Figure 2. Association and dissociation times of DSB protein.

a, Within-chromosome organization of Rec114 association and dissociation times (*ARS*+ strain). Each point is a called Rec114 peak. Green lines indicate binding duration (Δt). Vertical lines mark the per-chromosome means for association and dissociation.

b, Per-chromosome Rec114 and Mer2 binding duration in *ars*Δ strains. n = 1 time course for each strain.

c, Association times, dissociation times, and binding duration of Rec114 (*ARS*+ strain) at Rec114 peaks, broken down by chromosome. n = 998 Rec114 peaks. In all boxplots in this

study: thick horizontal bars are medians, box edges are upper and lower quartiles, whiskers indicate values within 1.5 fold of interquartile range, and points are outliers.

d, Rec114/Mer2 shows early association and late dissociation on short chromosomes and thus longer duration of binding. Values were grouped for the shortest three chromosomes and the other thirteen chromosomes ("long"). Numbers above brackets indicate p values from one-sided Wilcoxon tests.

e, Chromosome size dependency of Spo11-oligo distributions as a function of sampling time. n = 2 time courses.

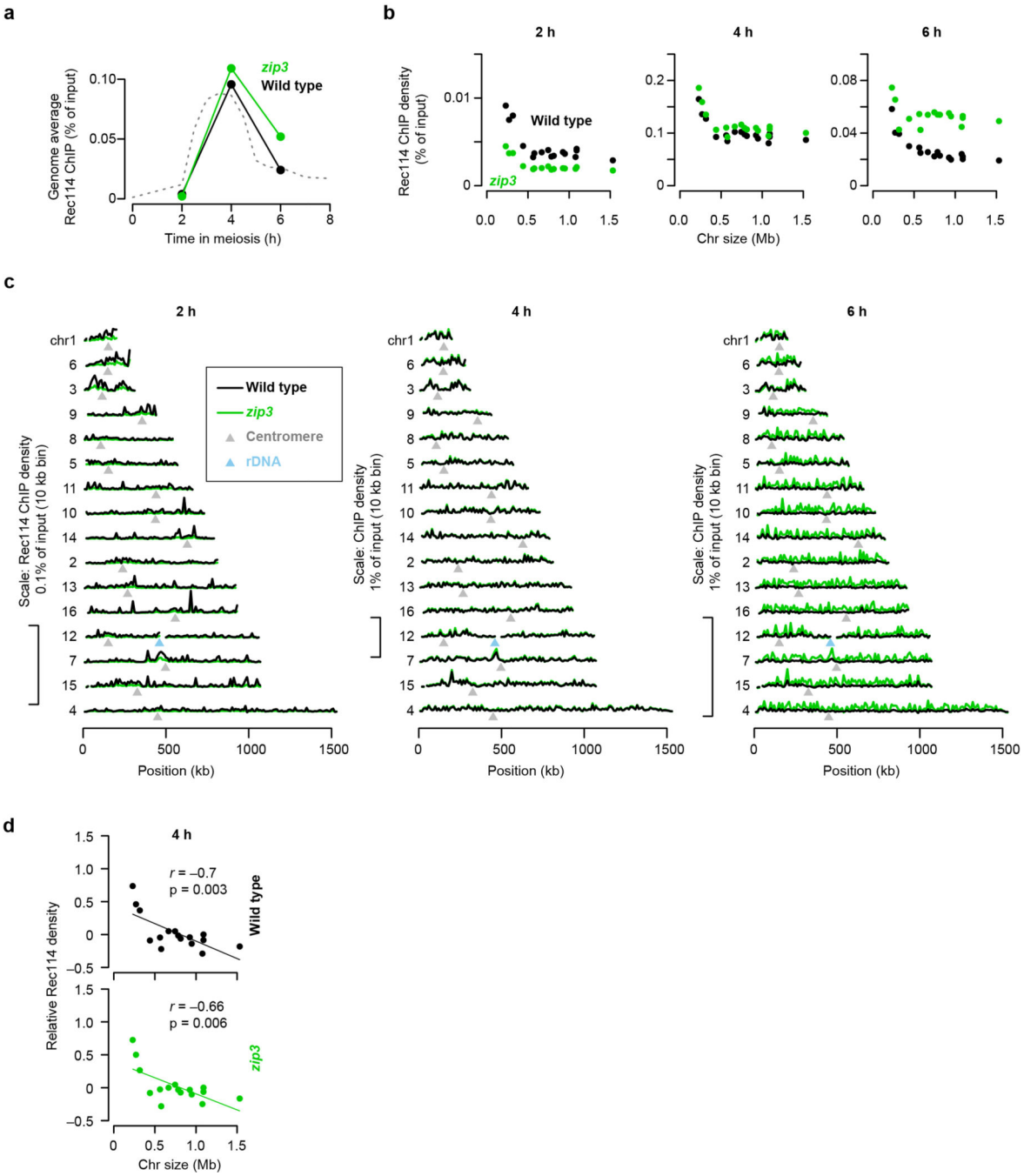

Extended Data Figure 3. Rec114 chromatin binding in the *zip3* mutant.

a, Genome-average Rec114 levels. Dashed line represents an independent wild-type profile from Fig. 1d.

b, Effects of *zip3* mutation on absolute Rec114 ChIP densities. ChIP-seq coverage was calibrated by qPCR. Each point is the mean for a single chromosome. At 2 h, which is very early in the initial accumulation phase of Rec114 on chromatin, the *zip3* mutant has ~;two-fold less Rec114 signal, affecting all chromosomes equivalently. It is possible that this decrease reflects a role for Zip3 early, but since Zip3 is not known to have any function this

early in prophase, a more likely explanation is that the *zip3* mutant culture lagged slightly behind the wild-type culture. At 4 h, Rec114 ChIP densities were very similar between the cultures, again with little or no difference between chromosomes. However, at 6 h, the *zip3* mutant retained substantially more Rec114 signal. At least some of this increase may be attributable to delayed meiotic progression because of inhibition of Ndt80[7,16], but importantly for purposes of this experiment, the Rec114 levels were disproportionately elevated on the 13 larger chromosomes. n = 1 time course for each strain.

c, Per-chromosome profiles of absolute Rec114 ChIP density.

d, Per-chromosome Rec114 ChIP density. This is the intermediate time point for the samples shown in Fig. 1h.

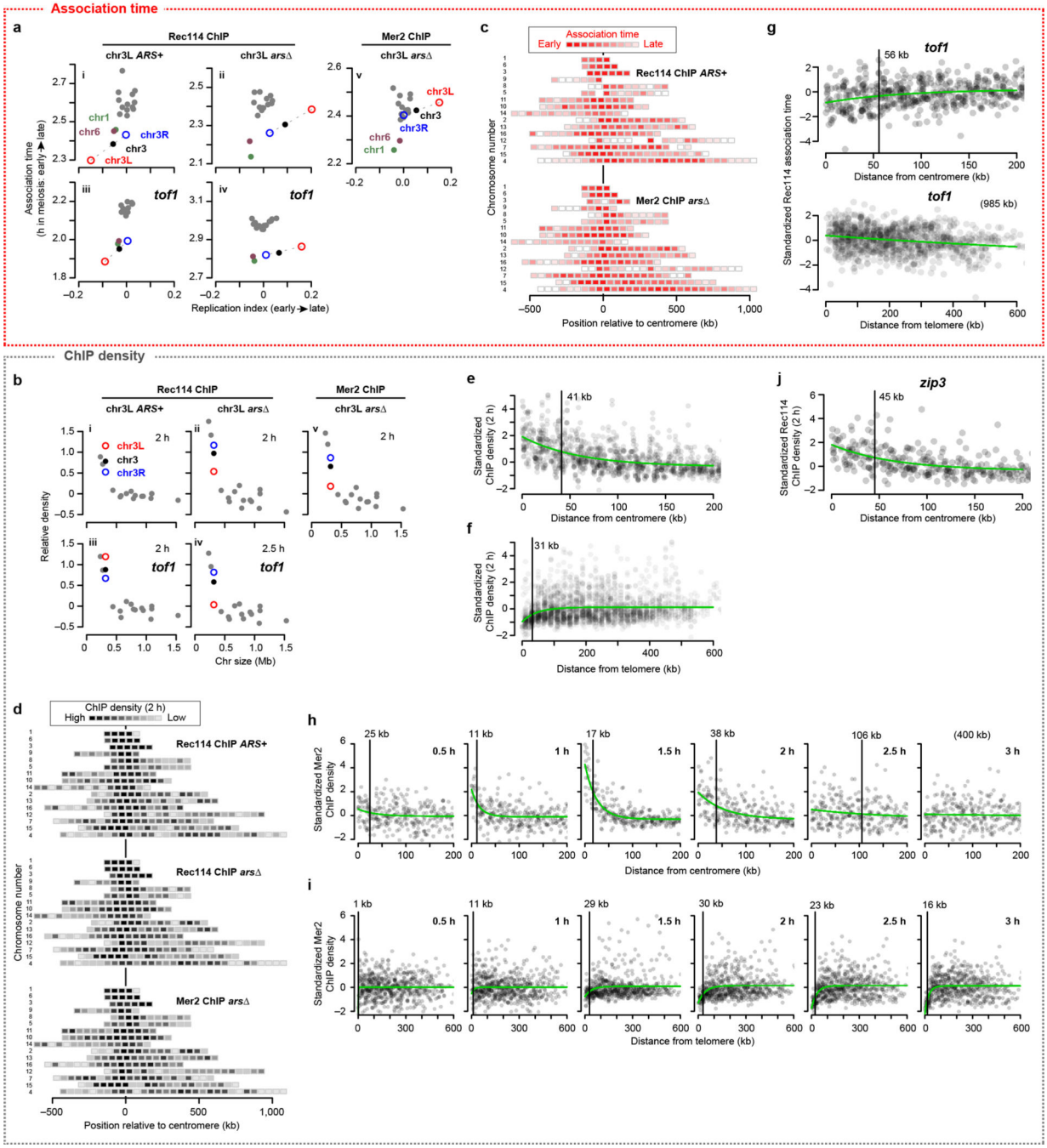

Extended Data Figure 4. Replication timing and the centromere and telomere effects.

a, b, Comparison of per-chromosome Rec114 and Mer2 association time (**a**) and ChIP density at early time points (**b**, 2 and 2.5 h, normalized to chr15) with replication timing. Replication index is defined as $-\log_2$ of the ratio of sequence coverages for ChIP input samples in S phase vs. G1 phase; lower values indicate earlier replication[18]. The means for the left arm (chr3L, open red circle) and right arm (chr3R, open blue circle) of chr3 are plotted separately, connected to the means for the entire chromosome (solid black) by dashed lines. In wild type, chr3L showed both early replication and early Rec114 association

(**a.i**). Origin deletion delayed replication and Rec114 association, but association was still on the early side compared with longer chromosomes despite extreme replication delay (**a.ii**). Mer2 was similar (**a.v**). Moreover, in *tof1*, the short trio still showed early Rec114 association (**a.iii**) and origin deletion delayed Rec114 association[18] less than it delayed replication (**a.iv**). ChIP densities exhibited a complementary trend: Rec114 and Mer2 overrepresentation on short chromosomes was partially dependent on early replication (**b**). Rec114 was naturally overrepresented on chr3L (**b.i**). Origin deletion caused a substantial decrease on chr3L but still left Rec114 at higher levels than on the larger chromosomes (**b.ii**) and Mer2 showed a similar pattern (**b.v**). In the *tof1* mutant, the short trio still showed high Rec114 signal (**b.iii**), and origin deletion reduced this signal on chr3L but left it in the higher part of the longer-chromosome range (**b.iv**). The similarity with Rec114 patterns, including much later Mer2 accumulation on the late-replicating left arm of chr3, suggests that Mer2 binding to chromatin is also coordinated with replication timing. Mer2 is able to bind chromatin in the absence of Rec114[3,6,40], but interaction with Rec114 (which is promoted by replication-associated Rec114 phosphorylation[18]) might stabilize or otherwise modify the localization of Mer2.

c, **d**, Intra-chromosomal distributions of Rec114 and Mer2 association times (**c**) and ChIP density at 2 h (**d**) in the indicated strains. **c**, Average values for 50-kb bins are presented as described in the legend to Fig. 2a. **d**, Each 50-kb bin is color-coded according to the mean ChIP density within the bin.

e, **f**, Centromere (**e**) and telomere (**f**) effects on ChIP density of DSB proteins at 2 h. The two Rec114 and one Mer2 ChIP time points were binned, standardized, and pooled as in Fig. 2b, c.

g, Centromere (top graph) and telomere (bottom graph) effects on Rec114 association time in *tof1* mutants. Rec114 ChIP-seq data from *ARS+ tof1* and *arsΔ tof1* strains were binned, standardized, and pooled as in Fig. 2b, c. The centromere and telomere effects are still apparent in the *tof1* mutants, but appear substantially weaker (particularly the telomere effect).

h, **i**, Detailed time courses of Mer2 binding to chromatin near centromeres (**h**) and telomeres (**i**).

j, The *zip3* mutation did not affect the centromere effect on Rec114 ChIP density at 2 h.

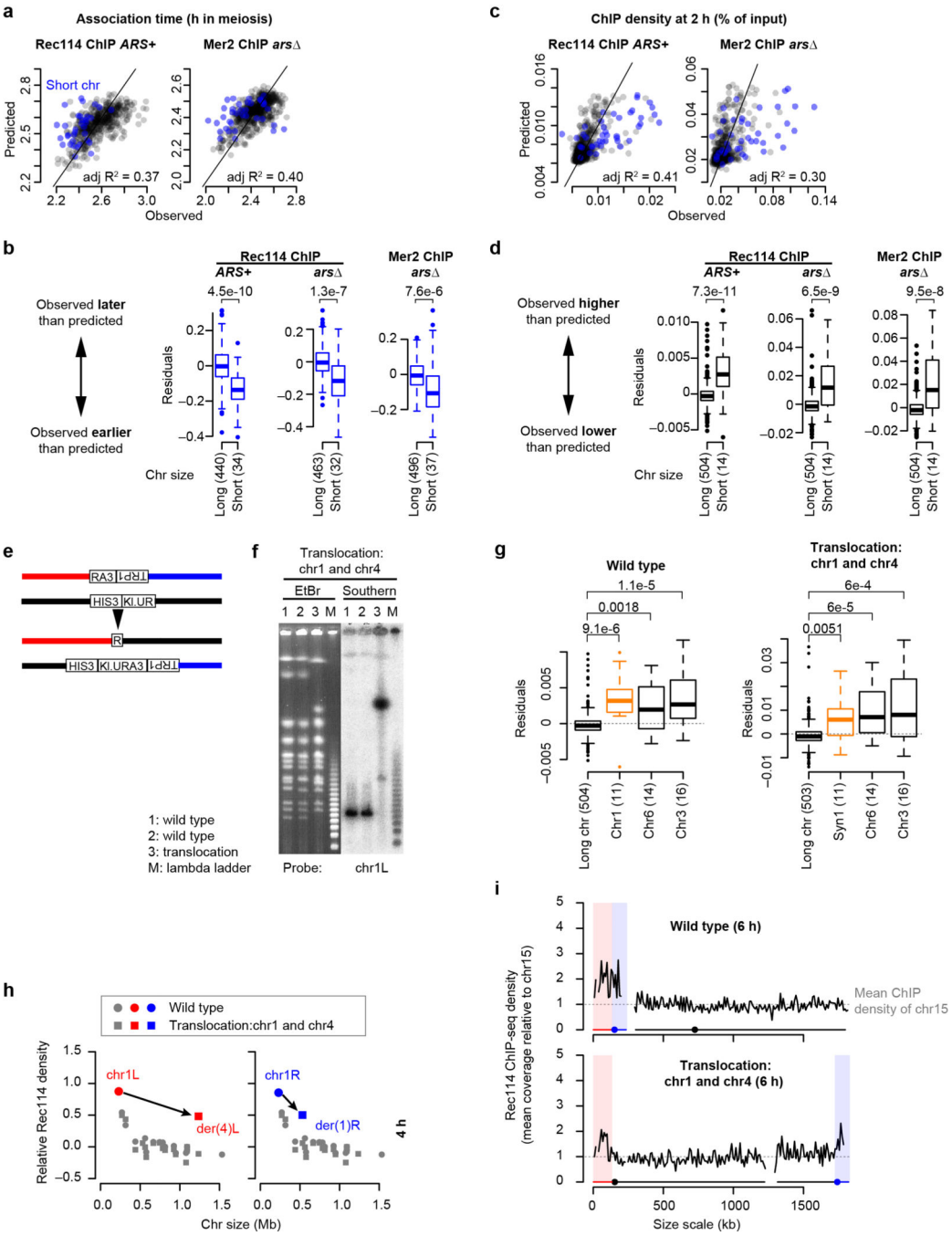

Extended Data Figure 5. DSB protein binding is boosting on smallest three chromosomes.

a, **c**, Results from multiple regression analyses using other Rec114 (*ARS*+) and Mer2 (*ars*Δ) ChIP-seq datasets performed as described in Fig. 2d, f to model Rec114 (n = 505 bins) and Mer2 (n = 583 bins) association times (**a**) as well as ChIP densities at 2 h (n = 597 bins) (**c**). Each point is a bin; bins on short chromosomes are blue.

b, **d**, Multiple regression models underperform on short chromosomes. Residuals from the three-factor models (**b**, association time; **d**, ChIP density) applied to each dataset in turn were grouped for the three shortest chromosomes vs. the rest except chr12 because of

exceptionally late association (Extended Data Fig. 2c). Numbers in parentheses indicate number of bins. P values are from one-sided Wilcoxon tests. Boxplots are as described in Extended Data Fig. 2c.

e–i, Effects of targeted translocations on per-chromosome Rec114 binding.

e, Strategy to target reciprocal translocation. To generate the translocation between chr1 and chr4, part of the 3′ end of the *URA3* gene from *Kluyveromyces lactis* ("*RA3*") was integrated on chr1 along with the *TRP1* gene. Separately, part of the 5′ end of *K. lactis URA3* ("*Kl.URA*") was integrated on chr4 along with the *HIS3* gene. The two parts of *K. lactis URA3* partially overlap, so their shared region of homology allows reciprocal recombination between them to result in formation of a functional *URA3* gene.

f, Confirmation of targeted translocations. High-molecular weight DNA was prepared from control and translocation strains and separated on pulsed-field gels and stained with ethidium bromide (EtBr). The translocations were then verified by Southern blotting using probes against the right and left ends of both chromosomes involved in the translocation (n = 4 different probes). A representative result using the chr1L probe is presented. For gel source data, see Supplementary Figure 1.

g, A three-factor multiple regression underperforms on chr1-derived sequences in both wild-type and translocation contexts. Boxplots show residuals from multiple regression performed as in **d** using the 2 h data. "Syn1" indicates sequence syntenic to chr1. Numbers in parentheses indicate number of bins. P values are from one-sided Wilcoxon tests.

h, Chr1-derived sequences retain high-level Rec114 binding when in a large-chromosome context. Per-chromosome Rec114 ChIP densities normalized to chr15 are shown at 4 h (the intermediate time point for the samples shown in Fig. 3b).

i, Rec114 profiles for wild-type and translocated chromosomes at 6 h. ChIP-seq data were normalized relative to chr15 and smoothed with a 10-kb sliding window.

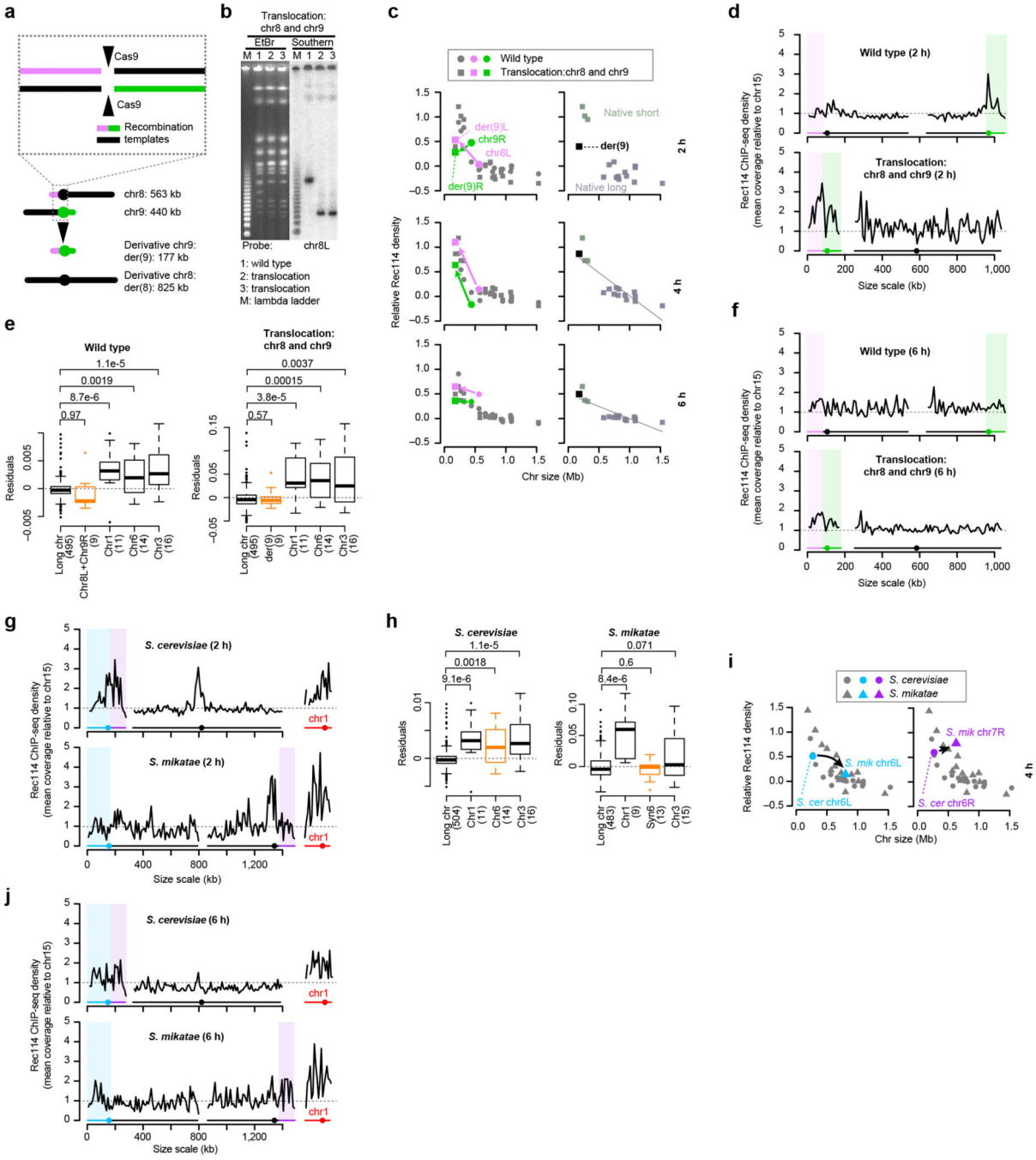

Extended Data Figure 6. An artificially short chromosome fails to acquire a boost in Rec114 binding.

a, Top: Strategy to target reciprocal translocation. To generate the translocation between chr8 and chr9, we introduced a plasmid expressing Cas9 and two guide RNAs that target cleavage within chr8 and chr9, respectively. This plasmid was introduced by co-transforming it along with 100 bp long recombination templates matching the desired reciprocal recombination products. Bottom: Targeted translocation between chr8 and chr9 (to scale).

b, Confirmation of targeted translocations as described in Extended Data Fig. 5f. The translocations were verified by Southern blotting using probes against the right and left ends of both chromosomes involved in the translocation (n = 4 different probes). A representative result using the chr8L probe is presented. For gel source data, see Supplementary Figure 1. **c**–**f**, Per-chromosome Rec114 ChIP densities (**c**), Rec114 profiles at 2 h and 6 h (**d**, **f**), and multiple regression residuals (**e**) are shown as Fig. 3b, c, and Extended Data Fig. 5g–i. In **e**, numbers in parentheses indicate number of bins. P values are from one-sided Wilcoxon tests. Boxplots are as described in Extended Data Fig. 2c.

g–j, High-level Rec114 binding to chr6-derived sequences is not retained in *S. mikatae*. Rec114 profiles (**g, j**), multiple regression residuals (**h**) and Rec114 ChIP density at 4 h (**i**) are shown as in Fig. 3b, c, and Extended Data Fig. 5g–i. In **h**, numbers in parentheses indicate number of bins. P values are from one-sided Wilcoxon tests. Note that the model also tended to underperform for chr3 in *S. mikatae*, but the distribution of residuals was not statistically significant (p = 0.071).

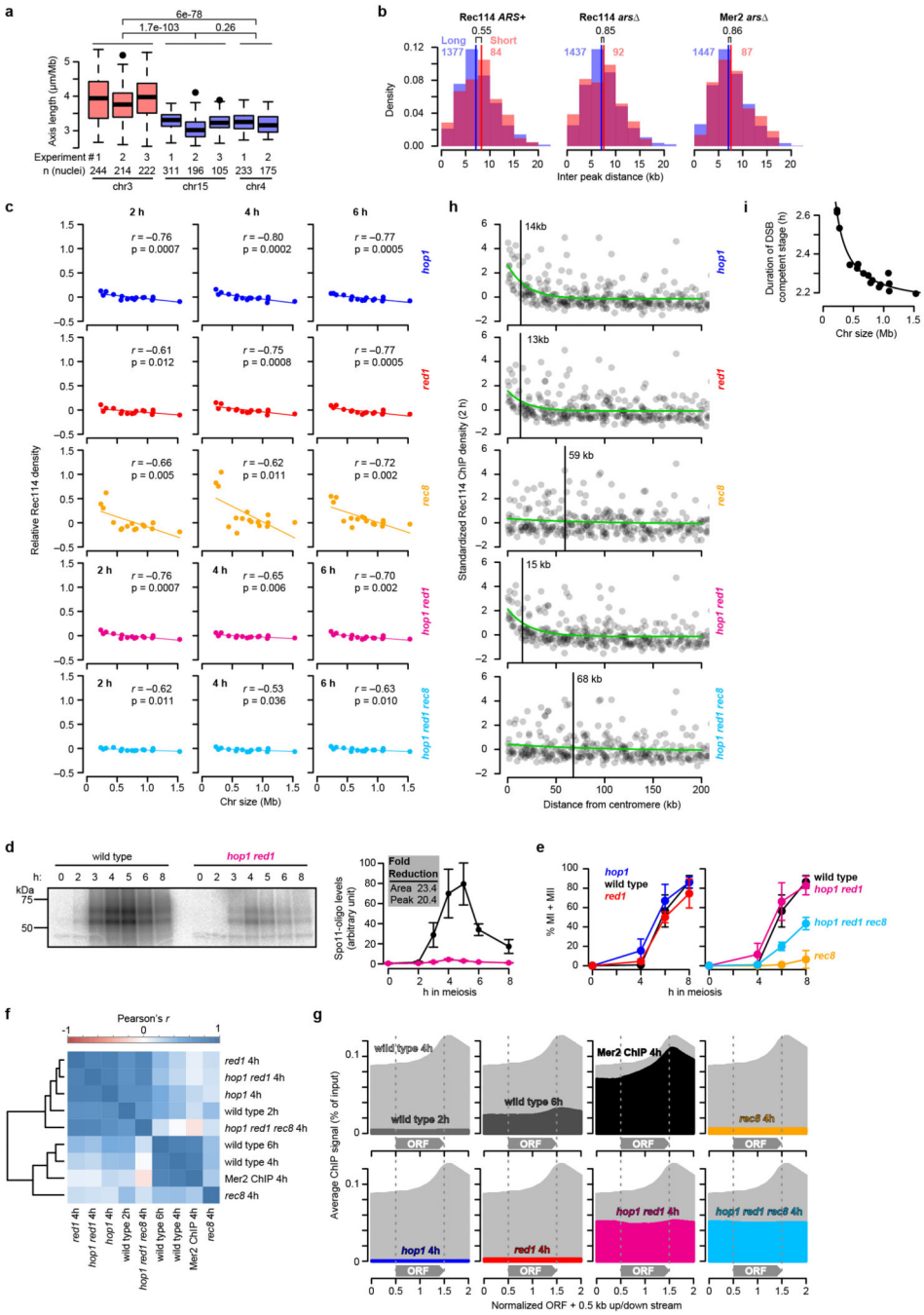

Extended Data Figure 7. Effect of chromosomes axis proteins on Rec114 chromatin binding patterns.

a, Long axes on chr3. To assess axis lengths, we used published measurements from Zhang, Kleckner et al. of synaptonemal complexes (SC) on pachytene chromosomes (Supplemental Table 1 from ref. [31]). In that study, spread, immunostained SCs were traced from the positions of *lacO* arrays (bound by LacI-GFP) integrated at the right end of chr3, chr4 or chr15 to the left end of each chromosome. We therefore used the SK1 genome assembly coordinates[41] of the *lacO* integration sites to estimate the nucleotide length corresponding to the SC measurement (0.30 Mbp for chr3, 1.48 Mbp for chr4, and 0.99 Mbp for chr15) and

calculated the per-Mbp axis lengths. Boxplots summarize results from eight independent experiments in wild type including SC length measured by Zip1 (experiments #1 and #2) or Rec8-HA (#3) staining. Note that the greater variance for chr3 is a consequence of the absolute measurement error (in μm) being a much larger fraction of the total chromosome length compared to the longer chromosomes. Data were pooled by chromosome for application of two-sided Wilcoxon tests. Boxplots are as described in Extended Data Fig. 2c.

b, Distributions of inter-peak distances. To ask if the preferential binding of DSB proteins on short chromosomes is due to presence of a higher density of DSB protein binding sites, we measured the distribution of the distances between DSB protein ChIP-seq peaks. Vertical bars indicate medians. Colored numerals above histograms indicate the number of distance measurements. Black numerals are p values from one-sided Wilcoxon tests. There was no significant difference ($p > 0.05$) between short and long chromosomes in any dataset, indicating that the density of preferred binding sites does not track with chromosome size. DSB protein binding sites correspond to sites where Hop1, Red1, and Rec8 are also enriched, i.e., presumptive sites where DNA is most likely embedded in the axis[3,42]. How then to reconcile the similar DSB protein binding site densities between short and long chromosomes with the longer per-Mbp axis length on chr3 (panel a)? Importantly, the preferred binding sites are defined on a population average basis. Therefore, one straightforward interpretation is that smaller chromosomes have more of their potential DSB protein binding sites axis-associated in each cell, while larger chromosomes are more likely to have loops that skip over preferred axis sites. This would yield smaller loop sizes and correspondingly longer axes on the short chromosomes despite a similar density of preferred axis sites per unit length of DNA.

c, Chromosome size dependence of Rec114 binding to chromosomes is lost in the absence of Hop1 or Red1, but not Rec8. Results are presented as in Fig. 4b. Note that, although correlations with chromosome size remain statistically significant in both the *hop1* and *red1* mutants, their slopes are negligible compared to wild type (Fig. 1e). n = 1 time course for each strain.

d, Spo11-oligo labeling to compare DSB levels between wild type and the *hop1 red1* double mutant. Flag-tagged Spo11 was immunoprecipitated from denaturing meiotic extracts, then Spo11-oligo complexes were end-labeled with terminal deoxynucleotidyl transferase and [α $-^{32}$P]-dCTP. Samples were separated on SDS-PAGE and imaged by phosphorimager. Spo11-oligo complexes in yeast run as two prominent bands reflecting different sizes of attached oligos[43]. Points and error bars represent mean and SD of three independent meiotic cultures. For gel source data, see Supplementary Figure 1.

e, Progression of meiosis in axis mutants. Samples from meiotic cultures were fixed and stained with DAPI, then fractions of cells completing meiosis I (MI) or both MI and meiosis II (MII) were counted. Identical wild-type data are presented in both panels to aid comparison. Points and error bars represent mean and SD of three independent meiotic cultures.

f, Correlation matrix of DSB protein ChIP data sets from wild type and axis mutants. n = 1 time course for each strain.

g, DSB protein distribution relative to open reading frames (ORFs). Using an R package provided by the Hochwagen laboratory[17], ORFs were standardized to a length of 1 kb, then ChIP-seq profiles were averaged over the standardized ORFs plus 0.5 kb of upstream and

downstream sequence. The 4 h wild-type pattern (light gray shading) is repeated in each panel to facilitate comparison.

h, The centromere effect is retained (albeit spreading less far) in *hop1* and *red1* single mutants but lost in *rec8* mutants. Rec114 ChIP data at 2 h were binned and standardized as in Fig. 2b. The *rec8* mutation was epistatic to *hop1 red1* for loss of the centromere effect.

i, The per-chromosome duration of DSB protein binding follows an inverse proportion relationship with chromosome size. Duration data from Fig. 1g and Extended Data Fig. 2b were combined, censoring the cold region between *CEN3* and *MAT*.

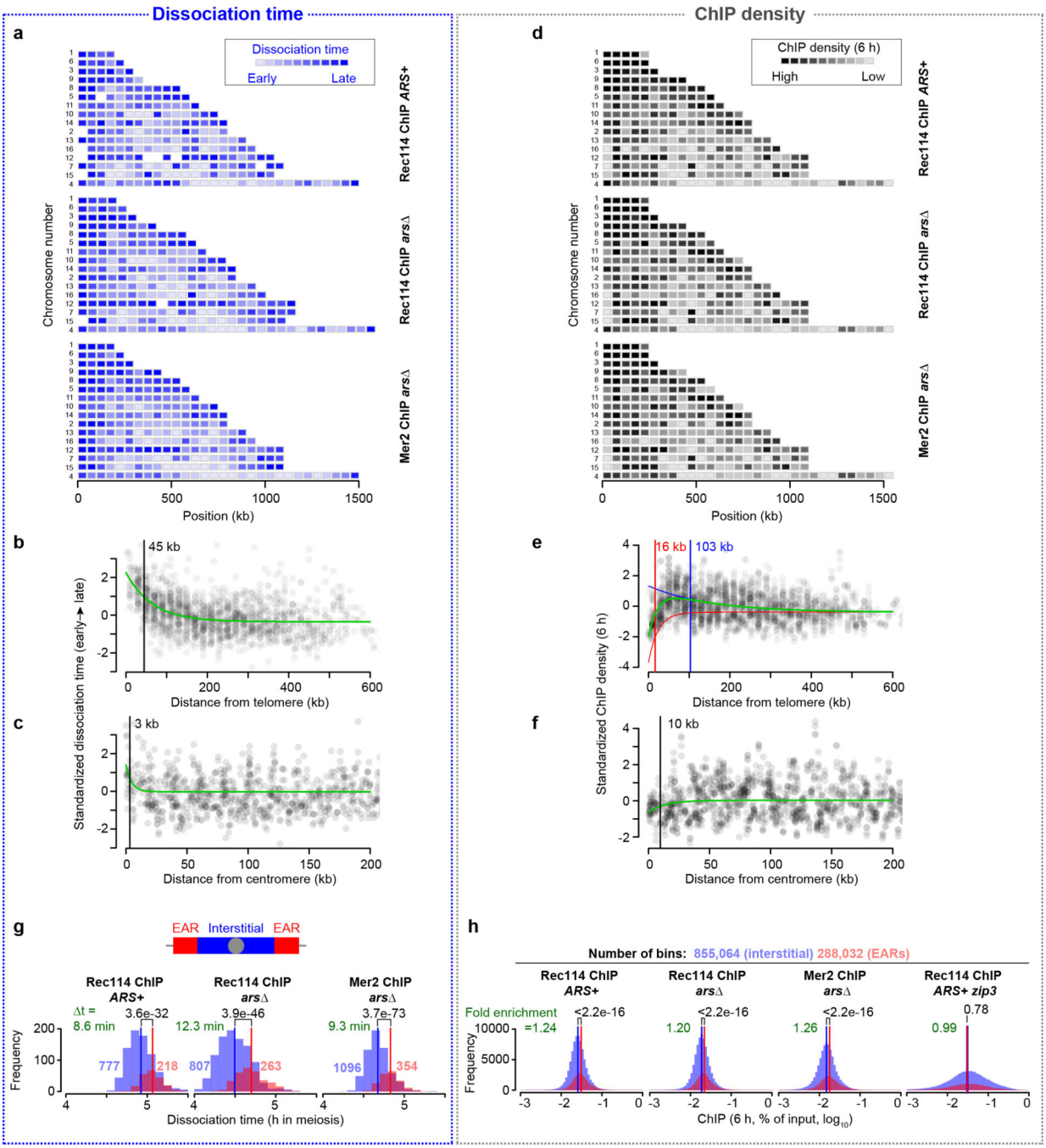

Extended Data Figure 8. Proximity to telomeres influences time and degree of DSB protein dissociation.

a, **d**, Intra-chromosomal distributions of Rec114 and Mer2 dissociation times (**a**) and ChIP density at 6 h (**d**) in the *ARS*+ and *ars*Δ strain. Each block represents a 50-kb bin color-coded according to the average of the Rec114 or Mer2 dissociation times for peak positions within the bin, or average ChIP density for the bin. Chromosomes are ranked by size, with the left chromosomal end at position zero.

b, c, e, f, Effects of proximity to centromere and telomere on dissociation time (**b**, **c**) and ChIP density (**e**, **f**) of DSB proteins. The two Rec114 and one Mer2 ChIP time courses were combined as follows. Dissociation time and ChIP density (6 h) data from three datasets were binned (20-kb windows), standardized, and plotted as in Fig. 2b, c and Extended Data Fig. 4e, f (grey dots). Green lines are fitted exponential models. Vertical bars indicate the distance where the effect decays to half of the original value. For the telomere effect modeling on ChIP density at 6 h (**e**), we instead fitted a composite curve (green line) consisting of two exponential models (red and blue lines) to describe repression and enrichment, respectively.

g, h, EAR effects on DSB protein dissociation time (**g**) and ChIP density at 6 h (**h**). Histograms show the distribution of dissociation time data at each peak position and ChIP density data binned in 10 bp windows located within EARs (defined as the regions from 20 to 110 kb from each telomere[33]) and interstitial regions (i.e., all segments between EARs). ChIP density data were log-transformed to decrease skewness. Numerals in red and blue indicate the numbers of peaks located within EARs and interstitial regions, respectively (**g**). P-values are from one-sided Wilcoxon tests (**g**) and one-sided t-tests (**h**).

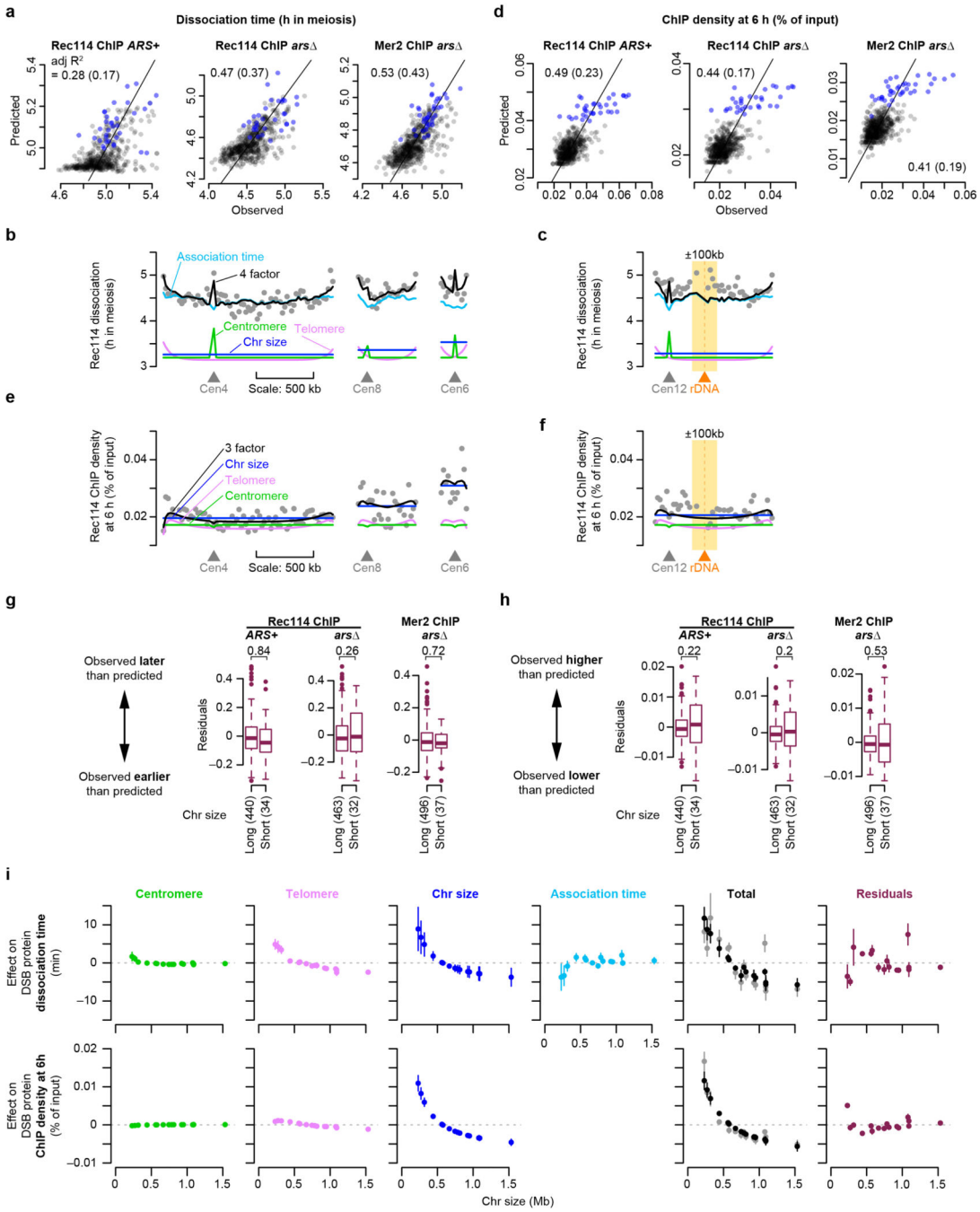

Extended Data Figure 9. Chromosome size, separate from EAR effects, is a major determinant of DSB protein behavior in late prophase.

a, **d**, A model incorporating association time, chromosome size, and the centromere and telomere effects. Association time, chromosome size, centromere, and telomere effects were binned in 20-kb windows and used as explanatory variables to model DSB protein dissociation time (**a**) or ChIP density at 6 h (**d**) by multiple linear regression. Association time was excluded in **d**. Each point compares the observed and model-predicted value within a bin. Bins on short chromosomes are blue. Adjusted R^2 values are shown for all data points

and (in parentheses) for only the longer chromosomes. Note that the fits for the ChIP density models are substantially worsened by removing the small chromosomes (panel d). This suggests that these models are mainly capturing between-chromosome differences rather than within-chromosome variation on the long chromosomes. n = 505, 539, and 583 bins for Rec114 ChIP *ARS*+, Rec114 ChIP *ars*Δ and Mer2 ChIP *ars*Δ datasets, respectively.

b, c, e, f, Examples of within-chromosome patterns predicted by the multiple regression model and each of its component factors. Gray dots are observed Rec114 dissociation times (**b, c**) or Rec114 ChIP density at 6 h (**e, f**) in 20-kb bins from the *ars*Δ strain. Blue, cyan, green, and magenta lines are the components chromosome size, association time, centromere, and telomere effects, respectively, and the black line is the prediction from the four-factor (**b, c**) and three-factor (**e, f**) regression models. The 200 kb surrounding the rDNA on chr12 is shaded yellow in panels c and f.

g, **h**, The multiple regression models do not underperform on the small chromosomes for DSB protein dissociation (**g**) or ChIP density at 6 h (**h**). Residuals from the regression models were grouped for the three shortest chromosomes vs. the rest except chr12. Numbers in parentheses indicate number of bins. P values are from one-sided Wilcoxon tests. Compare with the substantial underperformance on the smallest chromosomes of regression models applied to early DSB protein patterns (Extended Data Fig. 5b, d). Boxplots are as described in Extended Data Fig. 2c.

i, Size dependence and integration of each component shaping late DSB protein behavior (analogous to Fig. 4e). Net effects for each chromosome (relative to the genome-wide means) were estimated from the three-factor or four-factor models in panels a and d (points and vertical bars are means ± SD of the three data sets). Of particular importance for our purposes, note that a separate parameter capturing chromosome size per se dominates the models even when accounting for the telomere effect (which includes contribution of the EARs). This result suggests that, although EARs contribute to chromosome size-related differences in DSB protein dissociation[33], another size-related process(es) is quantitatively more important. Homologous pairing kinetics might be such a process[2,16,44]. See Supplementary Discussion 6 for further details.

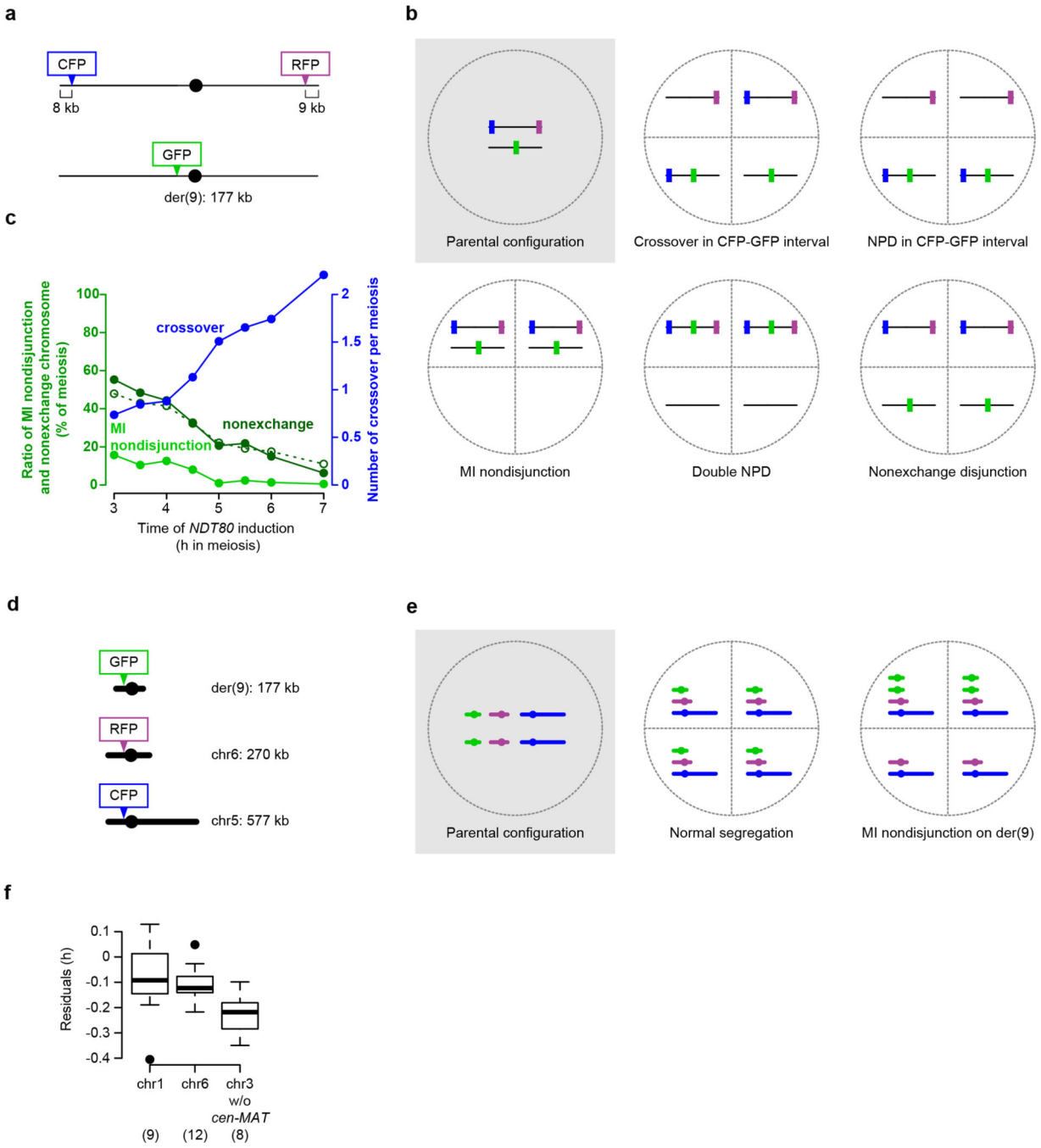

Extended Data Figure 10. Small chromosomes are at risk of chromosome missegregation.

a–c, Premature prophase I exit compromises crossing over and chromosome segregation on an artificial short chromosome. Panel a**, c**onfiguration of spore-autonomous fluorescent markers[39] used to detect crossovers and meiosis I (MI) nondisjunction of the artificial short chromosome (der(9), see Extended Data Fig. 6a–f). The strain also carries *NDT80* under the control of a galactose-inducible promoter (*P_{GAL}-NDT80*) and expresses the Gal4 transcription factor fused to a portion of the mammalian estrogen receptor (Gal4-ER)[45,46]. These constructs allow induction of Ndt80 expression at defined times by addition of β-

estradiol to the medium. Ndt80 expression is sufficient to drive exit from pachynema and prophase I (see Supplementary Discussion 8 for further detail). Note that this experimental set-up allows us to query a small chromosome that lacks the normal short-chromosome boost and to drive cells out of prophase before the homolog engagement pathway is allowed to operate fully to assure DSB formation. Panel b, schematics of chromosome segregation patterns with and without crossovers. NPD, nonparental ditype. Note that configuration of markers (crossover or nonexchange) cannot be determined in MI nondisjunction tetrads. Note also that double NPD tetrads are indistinguishable from MI nondisjunction; however, double NPDs are expected to be rare. Panel c, frequencies of MI nondisjunction and nonexchange (E0) chromosomes and average number of crossovers detected per meiosis. For E0, filled dark green circles are estimates of total E0 by combining observed E0 + observed MI nondisjunction; open circles are the predicted frequencies of E0 assuming a Poisson distribution with the observed mean number of crossovers per meiosis. Note the good agreement between these independent estimates of E0 frequency. β-estradiol was added at the indicated times, then chromosome segregation and crossing over were scored after the completion of meiosis and sporulation (54 h). Pachytene exit would normally begin to occur after ~;5 h in wild-type cells under these culture conditions[47]. Early induction of *NDT80* resulted in a decreased yield of crossovers and an increased frequency of chromosome missegregation, matching our expectation. The crossover and segregation defects were progressively attenuated the later *NDT80* was induced. Thus, delaying pachytene exit is sufficient to improve the likelihood of der(9) achieving a crossover. At least some of this improvement is likely to be attributable to providing more time in a DSB-permissive state, but other aspects of prophase chromosome pairing and recombination may also be facilitated.

d, e, Configuration of spore-autonomous fluorescent markers (**d**) and example segregation patterns (**e**) to detect MI nondisjunction for three different chromosomes. The strain also contained P_{GAL}-*NDT80* and Gal4-ER. Data are presented in Fig. 4f.

f, Residuals for each member of the shortest chromosome trio (not including the *CEN3–MAT* interval) from the three-factor multiple regression model applied to Rec114 association time (*ARS*+ dataset, Fig. 1f). The model performs poorly for all three chromosomes as noted in the main text, but performs especially poorly for the parts of chr3 that must have a high DSB frequency to balance the suppression of DSB formation in the *CEN3–MAT* interval. See Supplementary Discussion 9 for further detail. Numbers in parentheses indicate the number of bins. Boxplots are as described in Extended Data Fig. 2c.

Supplementary Material

Refer to Web version on PubMed Central for supplementary material.

Acknowledgments:

We are grateful to Agnès Viale and Neeman Mohibullah of the Memorial Sloan Kettering Cancer Center (MSKCC) Integrated Genomics Operation for DNA sequencing; Nicholas Socci at the MSKCC Bioinformatics Core Facility for mapping ChIP-seq and Spo11-oligo reads; and members of the Keeney laboratory, especially Shintaro Yamada for advice on data analysis and Laurent Acquaviva for sharing unpublished information. We thank Vijayalakshmi Subramanian (NYU), Andreas Hochwagen (NYU), and Franz Klein (Univ. of Vienna) for discussions and sharing unpublished information. We thank Michael Lichten (NCI), Ed Louis (Univ. of Nottingham), Kunihiro Ohta (Tokyo

Univ.), Angelika Amon (MIT), Wolfgang Zachariae (MPI of Biochemistry), Joao Matos (ETH Zurich), and Rodney Rothstein (Columbia Medical Center), for strains or plasmids.

Funding: IL and MvO were supported in part by National Institutes of Health (NIH) fellowships F31 GM097861 and F32 GM096692, respectively. This work was supported by NIH grants R01 GM058673 and R35 GM118092 to SK. MSKCC core facilities are supported by NCI Cancer Center Support Grant P30 CA008748.

References:

1. Hunter N. Meiotic Recombination: The Essence of Heredity. Cold Spring Harb Perspect Biol 7, doi:10.1101/cshperspect.a016618 (2015).
2. Keeney S, Lange J & Mohibullah N. Self-organization of meiotic recombination initiation: general principles and molecular pathways. Annu Rev Genet 48, 187–214, doi:10.1146/annurev-genet-120213-092304 (2014). [PubMed: 25421598]
3. Panizza S. et al. Spo11-accessory proteins link double-strand break sites to the chromosome axis in early meiotic recombination. Cell 146, 372–383, doi:S0092-8674(11)00758-6%5Bpii%5D10.1016/j.cell.2011.07.003 (2011). [PubMed: 21816273]
4. Arora C, Kee K, Maleki S & Keeney S. Antiviral protein Ski8 is a direct partner of Spo11 in meiotic DNA break formation, independent of its cytoplasmic role in RNA metabolism. Mol Cell 13, 549–559, doi:10.1016/s1097-2765(04)00063-2 (2004). [PubMed: 14992724]
5. Maleki S, Neale MJ, Arora C, Henderson KA & Keeney S. Interactions between Mei4, Rec114, and other proteins required for meiotic DNA double-strand break formation in Saccharomyces cerevisiae. Chromosoma 116, 471–486, doi:10.1007/s00412-007-0111-y (2007). [PubMed: 17558514]
6. Li J, Hooker GW & Roeder GS Saccharomyces cerevisiae Mer2, Mei4 and Rec114 form a complex required for meiotic double-strand break formation. Genetics 173, 1969–1981, doi:genetics.106.058768%5Bpii%5D10.1534/genetics.106.058768 (2006). [PubMed: 16783010]
7. Carballo JA et al. Budding yeast ATM/ATR control meiotic double-strand break (DSB) levels by down-regulating Rec114, an essential component of the DSB-machinery. PLoS Genet 9, e1003545, doi:10.1371/journal.pgen.1003545PGENETICS-D-12-02536%5Bpii%5D (2013).
8. Kumar R, Bourbon HM & de Massy B. Functional conservation of Mei4 for meiotic DNA double-strand break formation from yeasts to mice. Genes Dev 24, 1266–1280, doi:10.1101/gad.571710 (2010). [PubMed: 20551173]
9. Robert T. et al. The TopoVIB-Like protein family is required for meiotic DNA double-strand break formation. Science 351, 943–949, doi:10.1126/science.aad5309 (2016). [PubMed: 26917764]
10. Stanzione M. et al. Meiotic DNA break formation requires the unsynapsed chromosome axis-binding protein IHO1 (CCDC36) in mice. Nat Cell Biol 18, 1208–1220, doi:10.1038/ncb3417 (2016). [PubMed: 27723721]
11. Tesse S. et al. Asy2/Mer2: an evolutionarily conserved mediator of meiotic recombination, pairing, and global chromosome compaction. Genes Dev 31, 1880–1893, doi:10.1101/gad.304543.117 (2017). [PubMed: 29021238]
12. Mancera E, Bourgon R, Brozzi A, Huber W & Steinmetz LM High-resolution mapping of meiotic crossovers and non-crossovers in yeast. Nature 454, 479–485, doi:10.1038/nature07135 (2008). [PubMed: 18615017]
13. Chen SY et al. Global analysis of the meiotic crossover landscape. Dev Cell 15, 401–415, doi:10.1016/j.devcel.2008.07.006 (2008). [PubMed: 18691940]
14. Kaback DB, Guacci V, Barber D & Mahon JW Chromosome size-dependent control of meiotic recombination. Science 256, 228–232 (1992). [PubMed: 1566070]
15. Pan J. et al. A hierarchical combination of factors shapes the genome-wide topography of yeast meiotic recombination initiation. Cell 144, 719–731, doi:S0092-8674(11)00123-1%5Bpii%5D10.1016/j.cell.2011.02.009 (2011). [PubMed: 21376234]
16. Thacker D, Mohibullah N, Zhu X & Keeney S. Homologue engagement controls meiotic DNA break number and distribution. Nature 510, 241–246, doi:nature13120%5Bpii%5D10.1038/nature13120 (2014). [PubMed: 24717437]

17. Sun X. et al. Transcription dynamically patterns the meiotic chromosome-axis interface. Elife 4, doi:10.7554/eLife.07424 (2015).
18. Murakami H & Keeney S. Temporospatial Coordination of Meiotic DNA Replication and Recombination via DDK Recruitment to Replisomes. Cell 158, 861–873, doi:S0092-8674(14)00819-8%5Bpii%5D10.1016/j.cell.2014.06.028 (2014). [PubMed: 25126790]
19. Wojtasz L. et al. Mouse HORMAD1 and HORMAD2, two conserved meiotic chromosomal proteins, are depleted from synapsed chromosome axes with the help of TRIP13 AAA-ATPase. PLoS Genet 5, e1000702, doi:10.1371/journal.pgen.1000702 (2009).
20. Kauppi L. et al. Numerical constraints and feedback control of double-strand breaks in mouse meiosis. Genes Dev 27, 873–886, doi:gad.213652.113 [pii] 10.1101/gad.213652.113 (2013). [PubMed: 23599345]
21. Blitzblau HG, Chan CS, Hochwagen A & Bell SP Separation of DNA replication from the assembly of break-competent meiotic chromosomes. PLoS Genet 8, e1002643, doi:10.1371/journal.pgen.1002643PGENETICS-D-11-02760%5Bpii%5D (2012).
22. Kugou K. et al. Rec8 guides canonical Spo11 distribution along yeast meiotic chromosomes. Mol Biol Cell 20, 3064–3076, doi:10.1091/mbc.E08-12-1223 (2009). [PubMed: 19439448]
23. Borde V, Goldman AS & Lichten M. Direct coupling between meiotic DNA replication and recombination initiation. Science 290, 806–809, doi:8941%5Bpii%5D (2000). [PubMed: 11052944]
24. Fischer G, James SA, Roberts IN, Oliver SG & Louis EJ Chromosomal evolution in Saccharomyces. Nature 405, 451–454, doi:10.1038/35013058 (2000). [PubMed: 10839539]
25. Kellis M, Patterson N, Endrizzi M, Birren B & Lander ES Sequencing and comparison of yeast species to identify genes and regulatory elements. Nature 423, 241–254, doi:10.1038/nature01644 (2003). [PubMed: 12748633]
26. Lam I & Keeney S. Nonparadoxical evolutionary stability of the recombination initiation landscape in yeast. Science 350, 932–937, doi:10.1126/science.aad0814 (2015). [PubMed: 26586758]
27. Kleckner N. Chiasma formation: chromatin/axis interplay and the role(s) of the synaptonemal complex. Chromosoma 115, 175–194, doi:10.1007/s00412-006-0055-7 (2006). [PubMed: 16555016]
28. Acquaviva L. et al. Ensuring meiotic DNA break formation in the mouse pseudoautosomal region. bioRxiv, 536136, doi:10.1101/536136 (2019).
29. Kauppi L. et al. Distinct properties of the XY pseudoautosomal region crucial for male meiosis. Science 331, 916–920, doi:10.1126/science.1195774 (2011). [PubMed: 21330546]
30. Kleckner N, Storlazzi A & Zickler D. Coordinate variation in meiotic pachytene SC length and total crossover/chiasma frequency under conditions of constant DNA length. Trends Genet 19, 623–628, doi:10.1016/j.tig.2003.09.004 (2003). [PubMed: 14585614]
31. Zhang L. et al. Topoisomerase II mediates meiotic crossover interference. Nature 511, 551–556, doi:10.1038/nature13442 (2014). [PubMed: 25043020]
32. Blat Y, Protacio RU, Hunter N & Kleckner N. Physical and functional interactions among basic chromosome organizational features govern early steps of meiotic chiasma formation. Cell 111, 791–802, doi:10.1016/s0092-8674(02)01167-4 (2002). [PubMed: 12526806]
33. Subramanian VV et al. Persistent DNA-break potential near telomeres increases initiation of meiotic recombination on short chromosomes. Nat Commun 10, 970, doi:10.1038/s41467-019-08875-x (2019). [PubMed: 30814509]
34. Lange J. et al. ATM controls meiotic double-strand-break formation. Nature 479, 237–240, doi:nature10508%5Bpii%5D10.1038/nature10508 (2011). [PubMed: 22002603]
35. Zhang L, Kim KP, Kleckner NE & Storlazzi A. Meiotic double-strand breaks occur once per pair of (sister) chromatids and, via Mec1/ATR and Tel1/ATM, once per quartet of chromatids. Proc Natl Acad Sci U S A 108, 20036–20041, doi:1117937108%5Bpii%5D10.1073/pnas.1117937108 (2011). [PubMed: 22123968]
36. Gray S, Allison RM, Garcia V, Goldman AS & Neale MJ Positive regulation of meiotic DNA double-strand break formation by activation of the DNA damage checkpoint kinase Mec1(ATR). Open Biol 3, 130019, doi:rsob.130019%5Bpii%5D10.1098/rsob.130019 (2013).

37. Cooper TJ, Wardell K, Garcia V & Neale MJ Homeostatic regulation of meiotic DSB formation by ATM/ATR. Exp Cell Res 329, 124–131, doi:10.1016/j.yexcr.2014.07.016 (2014). [PubMed: 25116420]

38. Mohibullah N & Keeney S. Numerical and spatial patterning of yeast meiotic DNA breaks by Tel1. Genome Res 27, 278–288, doi:10.1101/gr.213587.116 (2017). [PubMed: 27923845]

39. Thacker D, Lam I, Knop M & Keeney S. Exploiting spore-autonomous fluorescent protein expression to quantify meiotic chromosome behaviors in Saccharomyces cerevisiae. Genetics 189, 423–439, doi:genetics.111.131326%5Bpii%5D10.1534/genetics.111.131326 (2011). [PubMed: 21840861]

40. Henderson KA, Kee K, Maleki S, Santini PA & Keeney S. Cyclin-dependent kinase directly regulates initiation of meiotic recombination. Cell 125, 1321–1332, doi:S0092-8674(06)00636-2%5Bpii%5D10.1016/j.cell.2006.04.039 (2006). [PubMed: 16814718]

41. Yue JX et al. Contrasting evolutionary genome dynamics between domesticated and wild yeasts. Nat Genet 49, 913–924, doi:10.1038/ng.3847 (2017). [PubMed: 28416820]

42. Blat Y & Kleckner N. Cohesins bind to preferential sites along yeast chromosome III, with differential regulation along arms versus the centric region. Cell 98, 249–259, doi:10.1016/s0092-8674(00)81019-3 (1999). [PubMed: 10428036]

43. Neale MJ, Pan J & Keeney S. Endonucleolytic processing of covalent protein-linked DNA double-strand breaks. Nature 436, 1053–1057, doi:nature03872%5Bpii%5D10.1038/nature03872 (2005). [PubMed: 16107854]

44. Mimitou EP, Yamada S & Keeney S. A global view of meiotic double-strand break end resection. Science 355, 40–45, doi:10.1126/science.aak9704 (2017). [PubMed: 28059759]

45. Benjamin KR, Zhang C, Shokat KM & Herskowitz I. Control of landmark events in meiosis by the CDK Cdc28 and the meiosis-specific kinase Ime2. Genes Dev 17, 1524–1539, doi:10.1101/gad.1101503 (2003). [PubMed: 12783856]

46. Picard D. in Nuclear receptors : a practical approach (ed Picard D.) 261–274 (Oxford University Press, 1999).

47. Murakami H, Borde V, Nicolas A & Keeney S. Gel electrophoresis assays for analyzing DNA double-strand breaks in Saccharomyces cerevisiae at various spatial resolutions. Methods Mol Biol 557, 117–142, doi:10.1007/978-1-59745-527-5_9 (2009). [PubMed: 19799180]

Methods References:

48. Reid RJ, Sunjevaric I, Keddache M & Rothstein R. Efficient PCR-based gene disruption in Saccharomyces strains using intergenic primers. Yeast 19, 319–328, doi:10.1002/yea.817 (2002). [PubMed: 11870855]

49. Bao Z. et al. Homology-integrated CRISPR-Cas (HI-CRISPR) system for one-step multigene disruption in Saccharomyces cerevisiae. ACS Synth Biol 4, 585–594, doi:10.1021/sb500255k (2015). [PubMed: 25207793]

50. Goldstein AL & McCusker JH Three new dominant drug resistance cassettes for gene disruption in Saccharomyces cerevisiae. Yeast 15, 1541–1553 (1999). [PubMed: 10514571]

51. Wach A, Brachat A, Pohlmann R & Philippsen P. New heterologous modules for classical or PCR-based gene disruptions in Saccharomyces cerevisiae. Yeast 10, 1793–1808 (1994). [PubMed: 7747518]

52. Carlile TM & Amon A. Meiosis I is established through division-specific translational control of a cyclin. Cell 133, 280–291, doi:S0092-8674(08)00283-3%5Bpii%5D10.1016/j.cell.2008.02.032 (2008). [PubMed: 18423199]

53. Neale MJ & Keeney S. End-labeling and analysis of Spo11-oligonucleotide complexes in Saccharomyces cerevisiae. Methods Mol Biol 557, 183–195, doi:10.1007/978-1-59745-527-5_12 (2009). [PubMed: 19799183]

54. Zhu X & Keeney S. High-Resolution Global Analysis of the Influences of Bas1 and Ino4 Transcription Factors on Meiotic DNA Break Distributions in Saccharomyces cerevisiae. Genetics 201, 525–542, doi:10.1534/genetics.115.178293 (2015). [PubMed: 26245832]

55. Scannell DR et al. The Awesome Power of Yeast Evolutionary Genetics: New Genome Sequences and Strain Resources for the Saccharomyces sensu stricto Genus. G3 (Bethesda) 1, 11–25, doi:10.1534/g3.111.000273 (2011). [PubMed: 22384314]

56. Schindelin J. et al. Fiji: an open-source platform for biological-image analysis. Nat Methods 9, 676–682, doi:10.1038/nmeth.2019 (2012). [PubMed: 22743772]

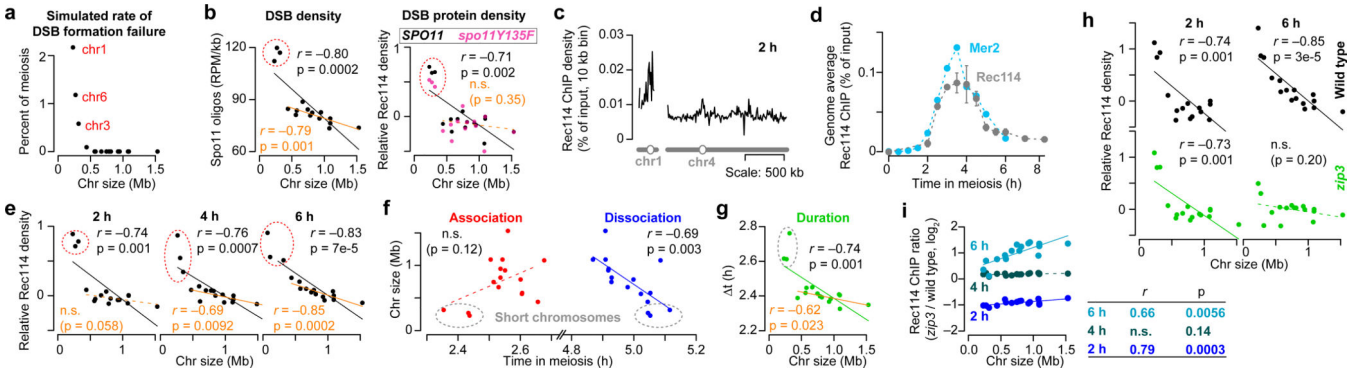

Figure 1. Rec114 and Mer2 accumulate preferentially on smaller chromosomes.

a, Random DSBs. For each simulation, 200 DSBs were distributed randomly by chromosome size; *S. cerevisiae* makes 150–200 DSBs per meiosis[15]. The plot shows the percent of simulations (10,000 total) in which the indicated chromosome failed to acquire a DSB.

b, Chromosome size dependence of DSBs (Spo11-oligo density in reads per million (RPM) per kb, 4 h, n = 28 maps), and Rec114 binding (ChIP-chip enrichment, 4 h, n = 1 culture for each strain). In all figures, chr12 is represented without including its full rDNA cluster. Data are from refs[3,38]. Relative Rec114 density: the mean ChIP signal for each chromosome was normalized to the mean for chr15 and $\log_2$-transformed. All correlations reported are Pearson's *r*.

c, Example Rec114 ChIP-seq for chr1 and chr4 at 2 h. Absolute ChIP signal was calibrated by qPCR and smoothed with 10-kb sliding window.

d, Time course of genome-average Rec114 and Mer2 levels. Gray points are mean ± range of two Rec114 datasets. Cyan points are from the single Mer2 dataset.

e, Size dependence of per-chromosome Rec114 ChIP density. The full time course is in Extended Data Fig. 1d.

f, Per-chromosome association and dissociation times for Rec114.

g, Per-chromosome Rec114 duration. Panels **c** and **e**–**g** are from the *ARS*+ time course (n = 1 culture); other time courses are in Extended Data Fig. 1 **and** 2.

h, i, Zip3-dependent homolog engagement shapes Rec114 abundance late in prophase. Graphs show per-chromosome Rec114 ChIP density (normalized to chr15) (**h**) and log fold change in the *zip3* mutant (**i**). n = 1 culture for each strain.

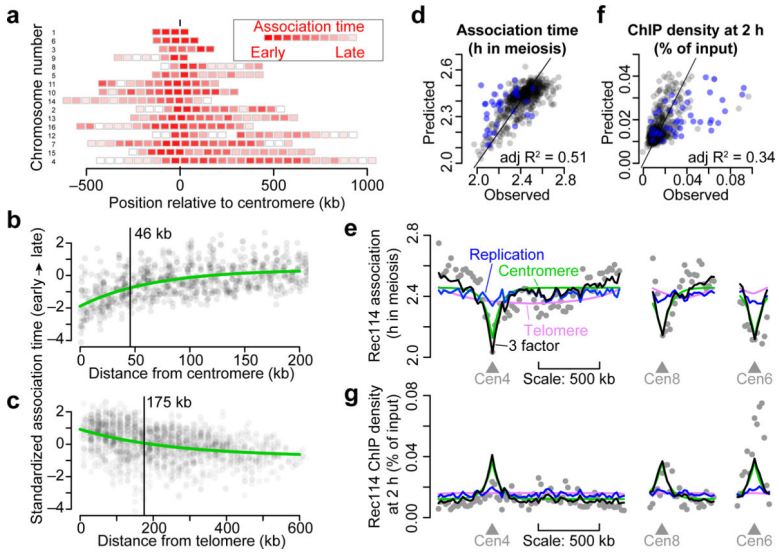

Figure 2. Replication timing and proximity to centromeres and telomeres influence time and amount of Rec114 association.

a, Intra-chromosomal distributions of Rec114 association times in the *ars*Δ strain. Each block is a 50-kb bin color-coded to the average Rec114 association times for peaks within the bin. Chromosomes are ranked by size, with centromere at position zero. See also Extended Data Fig. 4c, d).

b, c, Centromere (**b**) and telomere (**c**) effects on association time of DSB proteins. The two Rec114 and one Mer2 ChIP time courses were combined as described in Methods. Each point is the value from one dataset for a 20-kb bin. Darker color indicates overlapping points. Green lines are exponential fits. Vertical bars are distances where effects decay to half the original value.

d, **f**, Replication index and centromere and telomere effects were binned in 20-kb windows and used as explanatory variables to model Rec114 association time (**d**, n = 539 bins) or ChIP density at 2 h (**f**, n = 597 bins) in the *ars*Δ strain by multiple linear regression. Each point is a bin; bins on short chromosomes are blue.

e, **g**, Examples of within-chromosome patterns predicted by the multiple regression model and each of its component factors. Gray dots are average Rec114 association times (**e**) or Rec114 ChIP density at 2 h (**g**) in 20-kb bins, in *ars*Δ datasets. Blue, green, and magenta lines are the component replication, centromere, and telomere effects, respectively, and the black line is the prediction from the three-factor regression model.

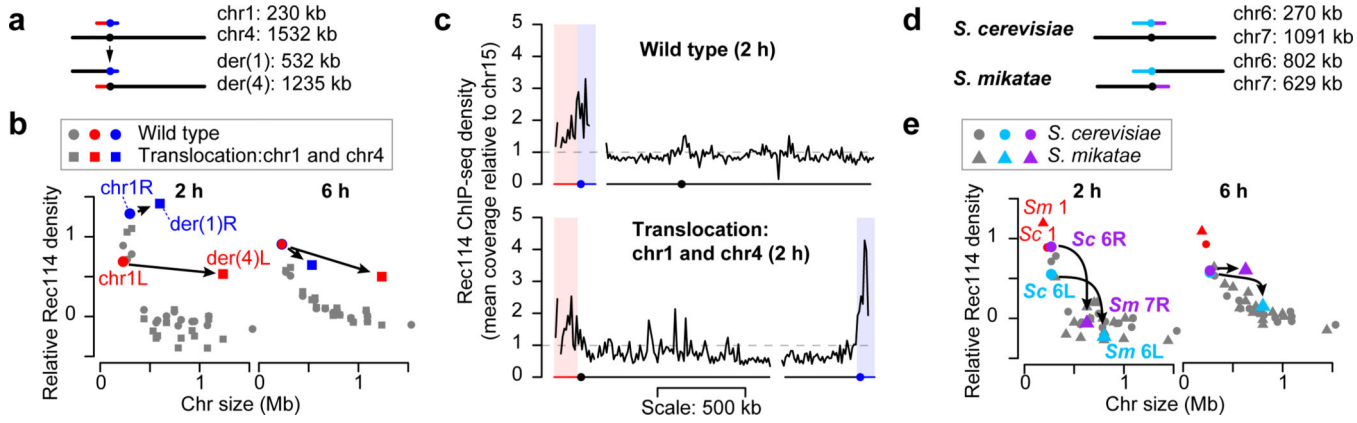

Figure 3. The Rec114 boost is intrinsic to short chromosomes.

a, Targeted translocation between chr1 and chr4 (to scale).

b, Chr1-derived sequences retain high-level Rec114 binding when in a large-chromosome context. Per-chromosome Rec114 ChIP densities normalized to chr15 are shown at 2 and 6 h.

c, Rec114 profiles for wild-type and translocated chromosomes. ChIP-seq data were normalized relative to chr15 (dashed line) and smoothed with a 10-kb sliding window.

d, e, Selective pressure has maintained the short chromosome boost on chr6. Shown are a to-scale schematic of syntenic regions on different-sized chromosomes in *S. cerevisiae* (Sc) and *S. mikatae* (Sm) (**d**) and per-chromosome Rec114 ChIP densities (**e**).

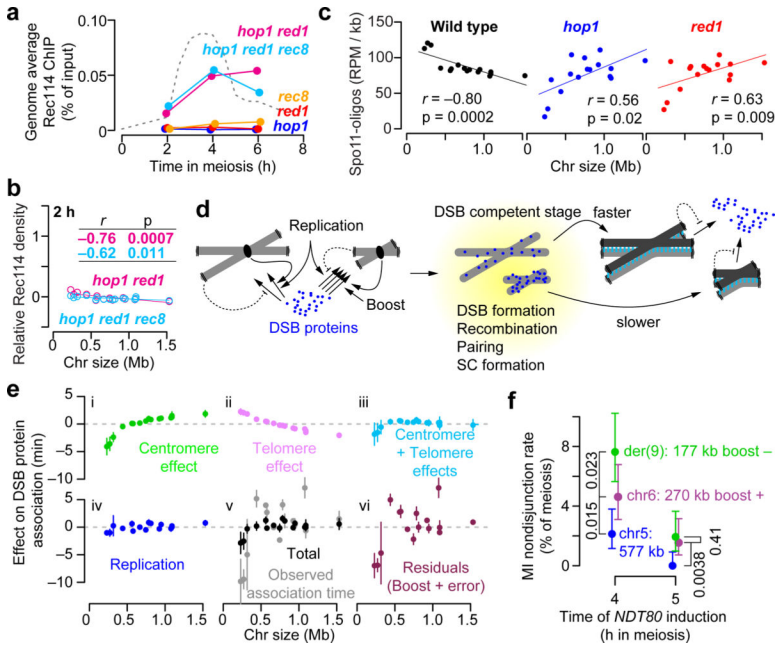

Figure 4. Role of axis proteins in the short chromosome boost and an integrated view of DSB control.

a, Genome-average Rec114 levels. Dashed line, wild-type profile from Fig. 1d.

b, Chromosome size dependence of Rec114 binding requires Hop1 and Red1. Although correlations with size are statistically significant, slopes are negligible compared to wild type (Fig. 1e).

c, Preferential DSB formation on small chromosomes is lost in *hop1* and *red1* mutants. Samples were collected at 4 h in meiosis. n = 28 (wild type), 2 (*hop1* and *red1*) independent maps.

d, Cartoon depicting the multiple pathways that govern DSB protein association and dissociation from long vs. short chromosomes.

e, Size dependence of each early pathway and their integration. Net effects for each chromosome (relative to mean association time) were estimated from the three-factor models in Fig. 2d and Extended Data Fig. 5a (points and vertical bars are means ± SD of the three data sets). Panels i–iii show centromere and telomere effects and their combination. Panel iv shows the effect of replication timing (high SD for chr3 is from *ars*Δ). Panel v merges all three pathways and compares this total to observed association time. Panel vi depicts what is not explained by these three pathways, inferred as the short chromosome boost. See Supplementary Discussion 4 for further details.

f, Small chromosomes are at greater risk of missegregation when DSB control is dysregulated. Chromosome missegregation was scored using spore-autonomous fluorescent reporters[39] (Extended Data Fig. 10d, e) in a strain with *NDT80* under inducible control. Premature *NDT80* expression (4 h, n = 563 tetrads) caused more missegregation for smaller chromosomes, especially for der(9) which lacks the small-chromosome boost. Segregation became more accurate when *NDT80* was induced later (5 h, n = 516 tetrads) to allow more time for DSBs to continue to accumulate; because of feedback tied to homolog engagement, longer time is predicted to provide greater benefit to smaller chromosomes, as was seen.

Error bars represent 95% confidence intervals. P values from one-sided Fisher's exact test are shown.